

Minimising Event Size, Maximising Physics: Inclusive Particle Isolation for LHCb's Run 3

Marta Calvi¹, Tommaso Fulghesu², George Hallett³, Luca Hartman^{4,5}, Basem Khanji⁶
Veronica S. Kirsebom^{1†}, Thomas Latham³, Marion Lehuraux³, Ching-Hua Li^{2†}, Abhijit
Mathad^{4†}, Matthew Monk^{3,7,8}, Andy Morris^{2†}, Matthew Scott Rudolph⁶, Francesca
Swystun⁷, Dorothea vom Bruch²

¹ *University of Milan-Bicocca, Milan, Italy*

² *Aix Marseille Univ., IN2P3/CNRS, CPPM, Marseille, France*

³ *Department of Physics, University of Warwick, Coventry, United Kingdom*

⁴ *European Organization for Nuclear Research (CERN), Geneva, Switzerland*

⁵ *Ecole Polytechnique Fédérale de Lausanne (EPFL), Lausanne, Switzerland*

⁶ *Syracuse University, Syracuse, New York, USA*

⁷ *Cavendish Laboratory, University of Cambridge, Cambridge, United Kingdom*

⁸ *School of Physics and Astronomy, Monash University, Melbourne, Australia*

[†] *Contact authors (alphabetic): V. S. Kirsebom, C. H. Li, A. Mathad, A. Morris.*

Keywords: High-energy-physics, LHCb experiment, Real-time trigger, Data Processing and Offline Analysis

Abstract

The Run 3 of the LHC brings unprecedented luminosity and a surge in data volume to the LHCb detector, necessitating a critical reduction in the size of each reconstructed event without compromising the physics reach of the heavy-flavour programme. While signal decays typically involve just a few charged particles, a single proton-proton collision produces hundreds of tracks, with charged particle information dominating the event size. To address this imbalance, a suite of inclusive isolation tools have been developed, including both classical methods and a novel Inclusive Multivariate Isolation (IMI) algorithm. The IMI unifies the key strengths of classical isolation techniques and is designed to robustly handle diverse decay topologies and kinematics, enabling efficient reconstruction of decay chains with varying final-state multiplicities. It consistently outperforms traditional methods, with superior background rejection and high signal efficiency across diverse channels and event multiplicities. By retaining only the most relevant particles in each event, the method achieves a 45% reduction in data size while preserving full physics performance, selecting signal particles with 99% efficiency. We also validate IMI on Run 3 data, confirming its robustness under real data-taking conditions. In the long term, IMI could provide a fast, lightweight front-end to support more compute-intensive selection strategies in the high-multiplicity environment of the High-Luminosity LHC.

Contents

1	Introduction	1
2	Classical Isolation Algorithms	5
3	Inclusive Multivariate Isolation (IMI)	6
3.1	Data samples	7
3.2	Signal and background classes	8
3.3	Input features	9
3.4	Training and performance	12
3.4.1	Comparison with Classical Isolation	15
3.4.2	Performance as a function of event multiplicity	16
3.4.3	Signal efficiency as a function of kinematic variables	18
4	Implementation and data size reduction	19
4.1	Integration into the LHCb selection framework	19
4.2	Data-size reduction and throughput	21
5	Validation in data	22
5.1	Ranking behaviour in real data	22
5.2	Reconstructing resonances using IMI-selected particles	24
5.3	Isolation efficiency in data and simulation	24
6	Summary and Outlook	24
	Acknowledgements	27
A	Inclusive simulation samples	27
B	Selection of prompt particles from excited b-hadron decays	27
C	Correlation matrix of input features for IMI	29
D	Signal and background efficiency as a function of isolation variables	31
	References	32

1 Introduction

A central challenge for the upgraded LHCb detector [1] during Run 3 (2022–2026) is to minimise the amount of data written to permanent storage while preserving the full physics potential of the experiment. The Large Hadron Collider (LHC) now delivers an instantaneous luminosity of up to $\mathcal{L} = 2 \times 10^{33} \text{ cm}^{-2}\text{s}^{-1}$ to the LHCb experiment, a five-fold increase compared to Run 2 (2015–2018). In addition, the upgraded LHCb detector is fully read out at the 30 MHz non-empty bunch-crossing rate and is processed by a software-only High-Level Trigger (HLT) [2–4].

At this input rate, the HLT reconstructs and selects¹ approximately $\mathcal{O}(250 \text{ kHz})$ of physics events. These are subsequently written to tape at a total data rate of around $\mathcal{O}(10 \text{ GB/s})$ [5]. These events are split across three data streams: TURBO, TURCAL, and FULL.

The TURBO stream, inspired by the model introduced in Run 2 [6, 7], stores only the online-reconstructed information relevant to the triggered signal, yielding a compact, analysis-ready format. It is used in two configurations: (i) *minimal* TURBO, which persists only the objects explicitly requested by the selection line, typically the signal candidate and essential metadata, and (ii) TURBO with *selective persistency* (TURBO(SP)), which additionally saves a controlled set of associated objects (e.g. vertices, PID quantities) according to per-line rules. The latter trades a modest increase in event size for greater offline flexibility. In contrast, the FULL stream retains the entire reconstructed event, enabling detailed offline analysis. For instance, in semileptonic b -hadron decays (final states containing one or more leptons), controlling backgrounds from partially reconstructed decays is essential. In such cases, the FULL stream enables direct reconstruction of these backgrounds, providing strong constraints on their shapes, yields, and associated systematics. The TURCAL stream further supplements the data by including raw detector information required for calibration tasks (e.g. PID). Because of their richer event content, FULL and TURCAL dominate storage bandwidth. As our work focuses on physics analyses, we specifically target events recorded in the FULL and TURBO streams.

To further reduce data volume, the SPRUCING framework [8] performs a second, centralised selection step that reduces the total output rate to approximately 3.5 GB/s written to disk. For the FULL stream in particular, the Technical Design Report (TDR) [5] mandates a reduction from 5.9 GB/s at the output of HLT2 to just 0.8 GB/s after sprucing [8]. Achieving this near eight-fold compression across $\mathcal{O}(10^3)$ Sprucing selection lines requires aggressive yet efficient pruning of event content.

The total data rate can be expressed as the product of two factors:

$$\text{Data-rate [MB/s]} \propto \underbrace{\text{event rate [kHz]}}_{\text{Hlt/Sprucing}} \times \underbrace{\text{event size [kB]}}_{\text{Hlt/Sprucing}}. \quad (1)$$

Therefore, reduction in the data rate can be achieved by either lowering the number of events retained (event rate) or by decreasing the amount of information stored per event (event size). Extensive efforts by the LHCb physics and performance working groups have addressed both strategies, developing high-efficiency reconstruction [9] and selection algorithms to retain not only the most “interesting” events, but also signal candidates

¹The HLT consists of a fast HLT1 stage with partial event reconstruction, followed by a HLT2 stage with full event reconstruction.

well-suited for fast offline analysis. This work advances the second component in Eq. (1), aiming to reduce the full event size through isolation algorithms that do more than just isolate signal decays, they selectively retain only the most relevant event information for detailed offline analysis.

A typical event at LHCb contains reconstructed charged and neutral particles, along with associated information such as primary vertices, trigger decisions, and a reconstruction summary. Figure 1 (top) shows the size composition of a representative FULL stream event used in semileptonic (SL) analyses. Only about 10% of the event size comes from metadata and the few particles of a partially reconstructed b -hadron decay. Neutral particles, mainly photons and neutral hadrons measured in the electromagnetic calorimeters, contribute roughly 35%. The largest share, nearly 55%, originates from reconstructed charged particles. As illustrated in figure 1 (bottom), these charged particles are classified into track categories according to the sub-detectors in which they leave hits. *Long* tracks deliver the best momentum resolution and precise vertex association. *Upstream* tracks correspond to low-momentum particles deflected by the magnet, while *Downstream* and *T* tracks are linked to long-lived decays such as K_S^0 or Λ . Finally, *VELO* tracks are essential for reconstructing the primary interaction vertices. Combined with particle-identification information from the Ring Imaging Cherenkov (RICH) detectors, this tracking data dominates the event size. This consideration leads us to the central question:

How can the relevant components of an event be identified efficiently, in a fast and inclusive manner, without introducing sensitivity to specific decay topologies or kinematic properties?

The core difficulty arises from *pileup*: multiple pp interactions per bunch crossing produce several primary (PVs) and secondary vertices (SVs), and the challenge is to associate reconstructed objects with the PV/SV that produced the signal hadrons. Inside the VELO, precise impact-parameter and vertexing information enable a largely geometric association to the correct vertex. Outside the VELO, however – after the magnet and into the downstream tracking stations, or when using RICH, calorimeter, or muon information – the association becomes far more difficult: longitudinal resolution degrades, magnetic deflection complicates back-extrapolation, and neutral objects lack track parameters altogether. Any strategy that reduces event size while preserving physics sensitivity must therefore identify and retain only the subset of objects *compatible with the signal PV/SV*, while rejecting contributions from other vertices and pileup activity.

This paper introduces an *Inclusive Multivariate Isolation* (IMI) algorithm specifically designed to address this association problem. Unlike classical isolation methods based on cones or vertexing, IMI evaluates and scores additional charged particles in the event, selecting only those most likely to originate from the same PV and decay chain as the signal candidate, while discarding the rest. As an illustrative example, consider the decay

$$B^0 \rightarrow D^{*-} \mu^+ \nu_\mu, \quad D^{*-} \rightarrow \bar{D}^0 \pi^-.$$
 (2)

In this case, the \bar{D}^0 and μ^+ form the *base* signal particles, while the π^- is an additional non-isolated particle that IMI is tasked to retain, enabling reconstruction of the D^{*-} state. By carefully selecting only the most relevant extra particles, IMI can significantly reduce the per-event size. Its design is therefore guided by the following key objectives:

- Deliver better background rejection than classical isolation techniques, particularly in high-pileup environments where traditional algorithms tend to degrade.

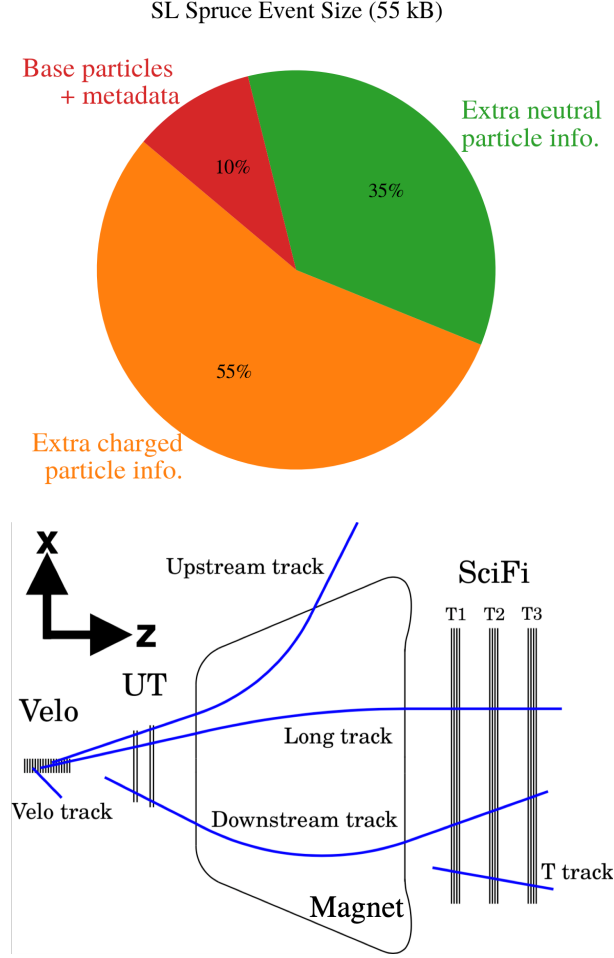


Figure 1: (Top) Event size breakdown for semileptonic FULL stream events in LHCb, based on a minimum-bias Run 3 simulation. The *base particles and metadata* include a few particles from a partially reconstructed b -hadron decay (e.g., D^0 and a muon), together with primary vertex, trigger, and reconstruction metadata. The *extra charged particle* component covers all other charged tracks (*Long*, *Downstream*, *Upstream*) and RICH PID information. Additional *VELO* and *T* tracks contribute 10% and 15% of the event size, respectively, and are not shown as they do not contribute to the Semileptonic event size. The *extra neutral particle* component corresponds to reconstructed neutrals, such as photons and neutral hadrons. (Bottom) Track categories in LHCb, defined by the tracking sub-detectors where hits are recorded [10].

- Enable applications beyond standard combinatorial suppression, including:
 1. Reconstruction of excited charm or charmless states involving particles from secondary decays, e.g. $B^0 \rightarrow D^{*-} \mu^+ \nu_\mu$, essential for precision tests of lepton-flavour universality [11, 12];
 2. Selection of data-driven control samples, such as the dominant background mode $\Lambda_b \rightarrow \Lambda_c^+ \mu^- \nu_\mu$, to isolate suppressed signal decays like $\Lambda_b \rightarrow p \mu^- \nu_\mu$, critical for probing CKM unitarity [13];
 3. Reconstruction of excited beauty-hadron states involving particles consistent with originating from the PV associated with the beauty hadron of interest, e.g., kaons in $B_{s2}^*(5840) \rightarrow B^+ K^-$, relevant for studies of lepton-flavour violation

(LFV) [12] and relative branching-fraction measurements [14].

- minimizing its impact on memory usage and on the overall event processing time (throughput), while remaining robust to variations in decay topology and kinematics.

As part of this work, classical isolation techniques were also developed for Run 3, including cone-based and vertex-based isolation, which remain widely used in many physics selections. Figure 2 shows the Run 3 data flow, including throughput and event rates for the different streams, and indicates where the classical isolation and IMI algorithms operate: the classical isolation runs in HLT2, whereas IMI is applied conservatively at the SPRUCING stage. The two approaches are independent, *i.e.*, selection lines using IMI do not rely on candidates preselected with the classical tool. As of the 2025 data-taking period, about 30% of selection lines across the TURBO and FULL streams use the classical isolation developed here, while IMI is employed in roughly 20% of SPRUCING selection lines targeting the FULL stream.

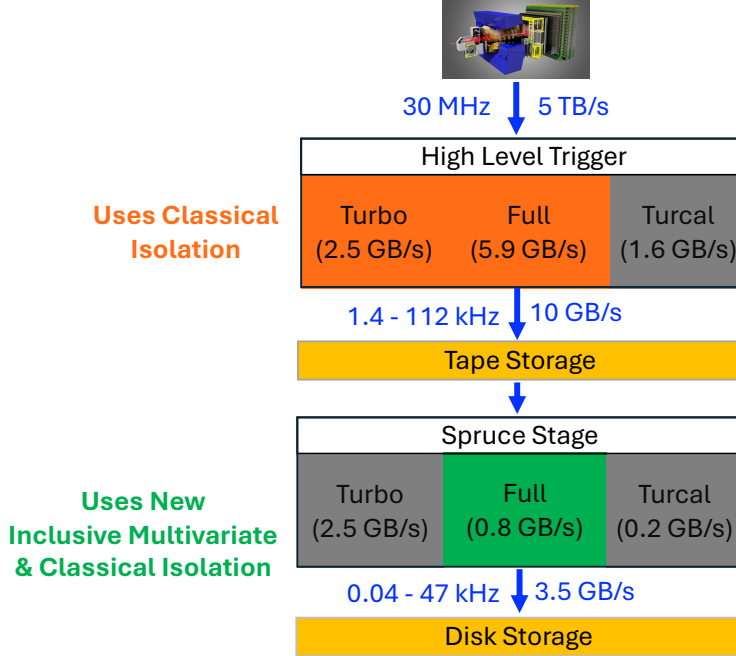


Figure 2: The LHCb data flow during Run 3, illustrating the throughput and event rates for different streams, and indicating where the classical and IMI isolation algorithms are applied. Note that none of the Spruce selection lines using IMI rely on candidates preselected with the classical isolation tool. Based on numbers from Ref. [5].

The paper is organised as follows. Section 2 reviews classical isolation techniques, Section 3 describes the IMI algorithm, compares its performance with classical methods, and studies its impact on key offline kinematic observables. Section 4 details the implementation of the classical isolation variants and the IMI algorithm, and quantifies their effect on data reduction. Section 5 presents validation of the IMI algorithm using Run 3 data. Conclusions and outlook are given in Section 6.

2 Classical Isolation Algorithms

The forward geometry of the LHCb detector, combined with its focus on low transverse momentum physics, results in approximately $\mathcal{O}(200)$ reconstructible charged tracks per inelastic pp interaction at Run 3 instantaneous luminosity. Isolating the few tracks, typically $\mathcal{O}(2-7)$, that originate from a heavy flavour signal decay in this dense environment is therefore essential, both for physics performance and for reducing data volume.

Over the past decade, three complementary charged particle isolation strategies have been developed and routinely employed at LHCb, as well as at the general-purpose LHC experiments and in other high energy physics experiments.²

Track isolation: Particles clearly associated with a primary vertex (PV) are rejected by requiring a large impact-parameter significance with respect to all the reconstructed PVs in the event, $\text{IP } \chi_{\text{PV}}^2 \gtrsim 16$, or an association with the same PV as the signal candidate (**samePV** flag). The impact parameter is defined as the minimum distance between the particle's trajectory and the given PV, while $\text{IP } \chi^2$ quantifies the change in the vertex-fit χ^2 when the track is included in the PV fit. It is also common to impose a second requirement: that the particle has a small impact-parameter significance with respect to the secondary vertex (SV) of the signal candidate, $\text{IP } \chi_{\text{SV}}^2$. Simple cut-based implementations of this approach were first developed by the DØ [15] and CDF [16] experiments, followed by ATLAS [17] and CMS [18]. The method was later adopted at LHCb for rare decay searches [19, 20] and for flavour-tagging algorithms [21]. Multivariate extensions, incorporating additional topological and kinematic features, as well as track-type information (*Long* and *VELO*) [22], were first introduced in $B_{(s)}^0 \rightarrow \mu^+ \mu^-$ analyses [23] and LFV studies [24], and they are also used in rare decay searches at ATLAS and CMS [25, 26]. A schematic representation of how the track isolation strategy works is shown in Fig. 3 (top).

Cone isolation: All reconstructed particles within a cone of radius

$$R = \sqrt{(\Delta\eta)^2 + (\Delta\varphi)^2}, \quad R \in [0.4, 0.5],$$

around the momentum direction of the signal candidate are considered. Here, $\Delta\eta$ and $\Delta\varphi$ denote the differences in pseudorapidity and azimuthal angle, respectively, both defined in the laboratory frame. Typical discriminants include the particle multiplicity inside the cone, the transverse momentum of the leading track $p_{\text{T}}^{\text{lead}}$, and the p_{T} asymmetry,

$$A_{p_{\text{T}}} = \frac{p_{\text{T}}(\text{sig}) - \left| \sum_{i \in \text{cone}} \vec{p}^i \right|_{\text{T}}}{p_{\text{T}}(\text{sig}) + \left| \sum_{i \in \text{cone}} \vec{p}^i \right|_{\text{T}}},$$

where the sum runs over the three-momenta \vec{p}^i of all particles in the cone, and the transverse component is taken only after the sum is formed. The variable approaches +1 for a perfectly isolated signal candidate. Cone-based variables are

²Neutral-particle isolation can also be built from electromagnetic (ECAL) and Hadronic (HCAL) clusters, but its contribution is not as large as charged-particle isolation (see Fig. 1). We therefore restrict the present IMI study to charged-particle isolation and leave the neutral case for future work, noting that classical isolation algorithms already support it.

fast and robust, and have seen widespread adoption in electroweak, jet, and heavy-flavour analyses [27–30], as well as in τ identification at ATLAS and CMS [31, 32]. However, their discriminating power tends to degrade in high-occupancy environments. Figure 3 (middle) provides a visual illustration of cone isolation.

Vertex isolation: Reconstructed tracks in the event that are not part of the signal candidate, but which pass loose track quality requirements, are combined with the signal candidate to form a common vertex. If the resulting vertex fit yields a χ^2/ndf below a specified threshold and the vertex is significantly displaced from the PV, the track is considered part of the decay chain. In fully reconstructed decays, cut-based isolation is often sufficient: if an additional track appears compatible with the decay chain, the candidate is more likely to originate from a partially reconstructed background than from signal, so genuine signal candidates are expected to have no such tracks. For partially reconstructed decays, by contrast, the situation is more complex and multivariate approaches have become standard [33, 34]. A schematic illustration of the vertex isolation strategy is shown in Fig. 3 (bottom).

Most LHCb analyses use classical techniques as standalone isolation tools, though in some cases two are combined: fast track-based isolation is typically deployed in the trigger, while the more computationally demanding vertex-based methods are applied offline, where their complementary strengths can be exploited. Each of the classical method provides good signal efficiency, but none achieves the required background rejection in the denser Run 3 environment, where the average number of reconstructible tracks per event has tripled compared to Run 2 [1].

3 Inclusive Multivariate Isolation (IMI)

Due to the limitations of classical isolation algorithms under high-pileup conditions, a multivariate isolation tool was developed integrating key features from all the three traditional approaches into a single classifier. As illustrated in Eq. (2), this classifier assigns a score to each combination constructed from a few *base* particles and an *extra* particle, to determine whether the extra particle should be classified as *isolated* or *non-isolated*. Non-isolated particles (those close to base particles) are more likely to originate from the signal decay and are retained for further analysis, particularly for reconstructing excited charm or charmless states, or for defining background-enriched control samples. Conversely, the IMI score can also be used as a discriminating variable to suppress backgrounds, such as combinatorial and partially reconstructed decays.

To ensure compatibility with the computational constraints of the Sprucing framework, several lightweight machine learning (ML) algorithms were explored, including Multi-Layer Perceptrons (MLPs), Random Forests, and Gradient Boosted Decision Trees (GBDTs). The Extreme Gradient Boosting (XGBoost) algorithm [35] was selected for its optimal balance between classification performance, computational efficiency, interpretability and strong performance on tabular high-energy physics data.

In the following sub-sections, we describe the data samples used for the training and validation of the IMI model, the selection of input features, and the performance of the IMI tool compared to classical isolation methods.

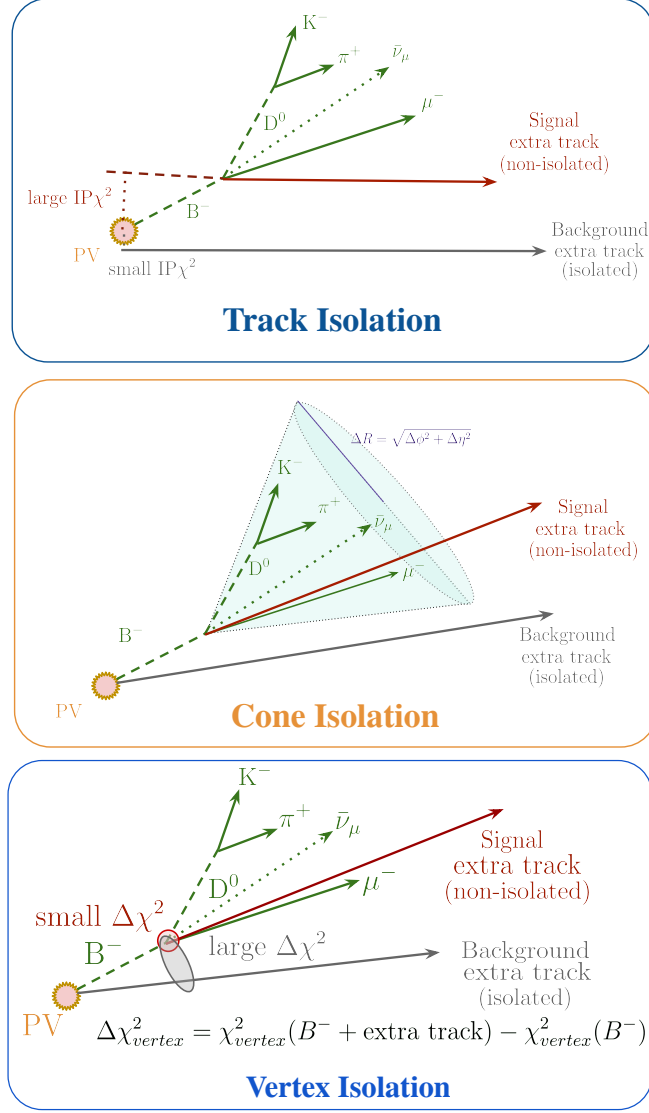


Figure 3: Schematic illustration of the three classical isolation strategies: track isolation (top), based on large impact-parameter significance; cone isolation (middle), based on the track’s proximity to the signal candidate; and vertex isolation (bottom), based on compatibility with the signal decay vertex. For clarity, the terms “Signal” and “Background” follow the definitions introduced in Section 3.2, while in the context of isolation the more general terminology “isolated” and “non-isolated” is always used.

3.1 Data samples

To ensure maximal inclusivity, the training sample consists of a broad cocktail of simulated semileptonic beauty-hadron decays, generated under nominal Run 3 LHCb conditions with an instantaneous luminosity of $2 \times 10^{33} \text{ cm}^{-2}\text{s}^{-1}$, corresponding to an average pile-up of $\mu = 5.3$ (visible interactions) or $\nu = 7.6$ total proton-proton interactions per bunch crossing. The sample spans a variety of initial states, B^0 , B^+ , B_s^0 , and Λ_b^0 , and final states containing electrons (e^\pm), muons (μ^\pm), or taus (τ^\pm), covering a wide kinematic phase space to avoid biasing the algorithm toward specific kinematic properties of the signal decay. These decay chains also include both short-lived intermediate states (e.g., $D_{(s)}^*$),

D^{**} , and Λ_c^*) and long-lived particles (e.g., D^0 , τ), enabling the isolation tool to learn how to disentangle contributions from both secondary and tertiary vertices. This diversity is essential to ensure that the IMI algorithm generalises robustly to the complex topologies expected in real LHCb data. A complete summary of the simulated decay modes used to train the IMI along with the definition of the *base* and *non-isolated* particles is provided in Appendix A in Table 1.

In all simulated decays, the base particles are required to be reconstructed as *Long* tracks and are selected with loose vertex, track quality and PID criteria to ensure they originate from a common decay vertex and are consistent with signal decays. The IMI tool currently targets non-isolated Long and Upstream tracks. Downstream tracks, which make up a relatively small fraction of all reconstructed tracks, were excluded due to their poorer momentum and vertex resolution, which limit their contribution to isolation performance. VELO tracks, expected to enhance signal efficiency, are planned for inclusion in future iterations.

3.2 Signal and background classes

The goal of the IMI tool is to identify charged particles that genuinely originate from the decay of a heavy-flavour hadron, while rejecting the far more numerous background particles unrelated to the signal decay. Signal particles are defined as those produced in the decay of a beauty hadron, which typically travels about ~ 1 cm from the PV before decaying within the LHCb acceptance. These signal particles fall into two categories:

- (a) those produced at the displaced secondary and tertiary vertex of the b -hadron decay, and
- (b) those originating from prompt strong decays of excited beauty states, such as $B_{s2}(5840) \rightarrow B^+ K^-$, where the kaon is emitted at the PV, while the B^+ continues to travel and decays further downstream.

The background consists of all other charged particles in the event that are kinematically and topologically uncorrelated with the signal decay. These include:

- (c) particles produced at or near the PV, predominantly from the soft-QCD hadronisation of light quarks and gluons in the underlying event.
- (d) particles originating from the decay of the second b -hadron in the event, which often forms the dominant combinatorial background due to their similar displaced-vertex signatures but lack of correlation with the signal vertex.

An illustration of the definitions of signal and background particles, defined in the above manner, is shown in Fig. 4.

An architecture was briefly explored categorising outputs into four classes, designed to disentangle all the above categories using inclusive $b\bar{b}$ simulation samples [36]. In practice, the multiclass network delivered no measurable gain: the limited statistics available for categories (b) and (d) prevented the model from learning boundaries more precise than those already captured in a simpler binary formulation. Therefore, a two-class IMI classifier was adopted, optimised to separate long-lived b -hadron decays from background. Prompt decays of excited b -hadrons are instead treated with a dedicated

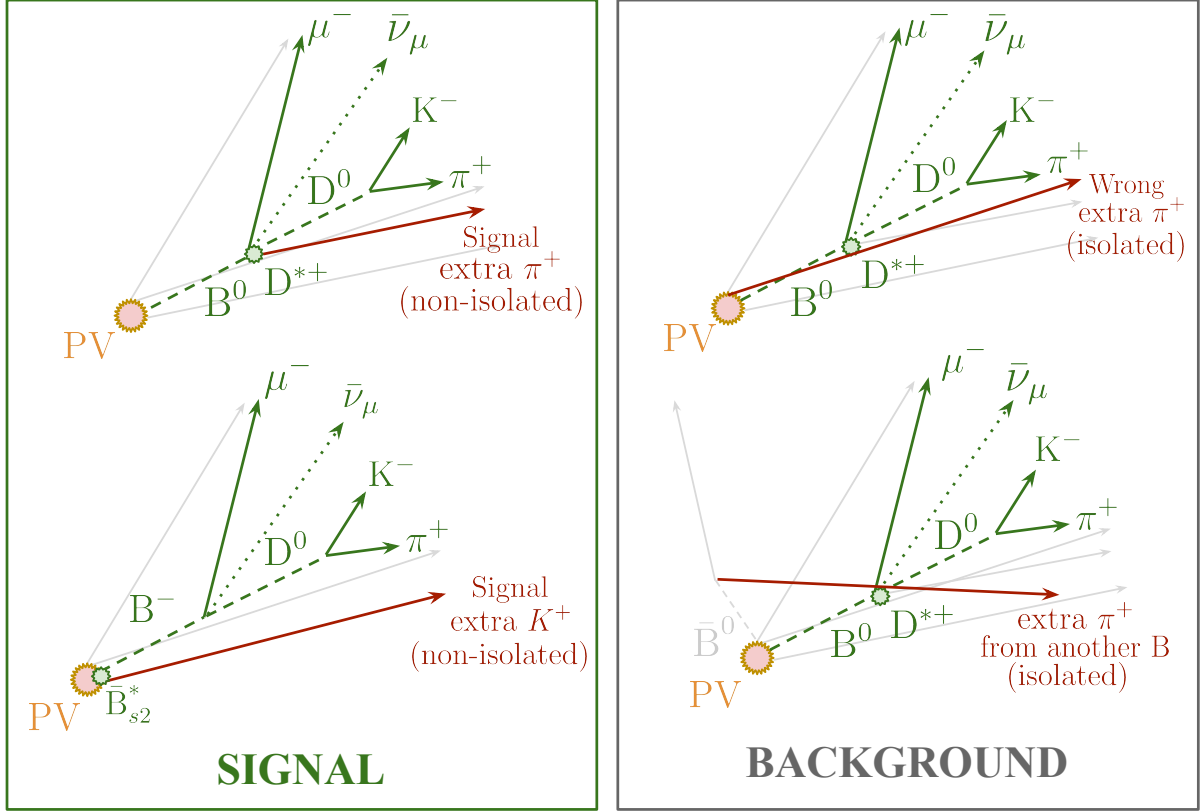


Figure 4: Illustration of typical signal- and background-like topologies relevant to the IMI tool. The depicted $B_s^* \rightarrow BK$ decay is shown as an illustrative example and was used only in the development of the cut-based method. In the left diagram, the signal candidates include non-isolated particles originating from the decay vertex of a b-hadron or its higher excited state. In the right diagram, the background candidates are defined as those formed by pairing with particles originating from the primary vertex or other b-hadrons in the event.

cut-based selection, described in Appendix B. Future versions, trained on larger and more diverse simulated samples, may revisit the multiclass strategy to exploit finer distinctions among these categories.

3.3 Input features

The IMI tool was initially trained with a broad set of input variables inspired by classical isolation algorithms widely used in the literature. These inputs, combining elements of the three traditional isolation strategies, provided a natural starting point that captured their complementary strengths. The feature set was then iteratively refined to maximise separation power between signal and background while reducing redundancy and avoiding biases in key physics observables. Particular attention was given to performance under high-pileup conditions: variables offering only marginal gains in such environments were discarded, while those showing consistent improvements across exclusive channels were retained. To protect the integrity of downstream measurements, features strongly correlated with decay kinematics were excluded, preventing distortions in sensitive distributions such as q^2 . The final feature set comprises variables probing angular and directional

correlations, impact parameters, vertex compatibility, displacement observables, and basic kinematics, as described below.

Impact parameter wrt PV ($\chi_{\text{IP wrt PV}}^2$): The impact parameter (IP) χ^2 of the additional signal particle with respect to the PV, effectively distinguishes particles produced at the PV from those originating from the decay of long-lived b -hadrons, which typically exhibit large impact parameter significance. It is less effective at separating signal from background particles produced in the decay of the other b -hadron in the event.

Impact parameter wrt SV ($\log(\chi_{\text{IP wrt SV}}^2)$): Analogous to the previous variable, but computed with respect to the secondary vertex (SV) reconstructed from the base particles. Signal particles from long-lived b -hadron decays are expected to be consistent with the SV, resulting in low IP significance, while background particles, particularly those from other b -hadron decays, exhibit higher values. Particles originating from tertiary decays, such as those of D mesons or τ leptons, may also show increased values, leading to partial overlap with background distributions.

Cone angular separation (*Transformed* ΔR): Defined as $\Delta R = \sqrt{(\Delta\eta)^2 + (\Delta\phi)^2}$, where $\Delta\eta$ and $\Delta\phi$ are the differences in pseudorapidity and azimuthal angle between the additional and base particles in the laboratory frame. Signal particles tend to be spatially correlated with the base system (small ΔR), whereas background particles are more widely dispersed. To enhance sensitivity in the low-angle regime where signal dominates, we apply a transformation: $(\Delta R)^{0.2}$.

Direction angle wrt flight direction (*Transformed* $DIRA$): The cosine of the angle α is computed between the momentum direction of the signal candidate, formed from the base and extra particle (\hat{p}), and its flight direction, defined by the displacement from the PV to the candidate's SV (\vec{FD}): $\cos \alpha = \hat{p} \cdot \vec{FD}$. The true b -hadrons tend to be aligned with the flight direction, yielding large values of $\cos \alpha$. We apply the transformation $(1 - \cos \alpha)^{0.2}$ to enhance separation in the region of small angular deviation.

Secondary vertex displacement (*SV signed distance*): When refitting the base candidate together with an additional track, we define the signed displacement between the two SV fits as

$$\Delta \vec{r}_{\text{SV}} \equiv \vec{r}_{\text{SV}}^{\text{base+trk}} - \vec{r}_{\text{SV}}^{\text{base}}, \quad d_{\text{SV}}^{\text{signed}} \equiv \text{sign}(\Delta r_{\text{SV},z}) |\Delta \vec{r}_{\text{SV}}|.$$

Here, $\vec{r}_{\text{SV}}^{\text{base}}$ is the decay vertex of the base candidate and $\vec{r}_{\text{SV}}^{\text{base+trk}}$ is the decay vertex after adding the extra track; $\Delta r_{\text{SV},z}$ denotes the z -component of the displacement. For correctly associated tracks (signal-like), the refit leaves the vertex essentially unchanged, so $d_{\text{SV}}^{\text{signed}}$ is sharply peaked at 0 with a width set by the SV-fit resolution. For misassociated tracks (typically prompt tracks from a PV), the common-vertex fit compromises between downstream decay tracks and a prompt line pointing back to a PV. This tends to pull the refitted SV upstream in z , yielding a broad distribution with an enhanced negative tail ($d_{\text{SV}}^{\text{signed}} < 0$), though both signs are possible depending on geometry and track covariances.

Distance of closest approach significance ($\log \chi_{\text{DOCA}}^2$): The variable $\log \chi_{\text{DOCA}}^2$ is defined as the natural logarithm of the DOCA significance between an additional particle and a base particle. Here, χ_{DOCA}^2 is the increase in the vertex-fit χ^2 when the two objects are constrained to a common vertex, or equivalently the squared, covariance-weighted separation at their points of closest approach (POCAs), defined as the locations along the trajectories where their distance is minimized. For a base particle that is a track, both particles are approximated as short straight lines using their fitted directions at the POCA. If the base particle is a composite, it is instead represented by a straight line drawn from its decay vertex in the direction of its reconstructed momentum.

For a base particle corresponding to a track, both objects are approximated as locally straight lines, defined by their fitted positions and directions extrapolated to the region near the point of closest approach (POCA). A composite base particle, on the other hand, is represented by its flight line from the decay vertex along its reconstructed momentum.

This variable provides good discrimination: true signal particles produced directly at the secondary vertex typically yield small values, particles from long-lived intermediate states (e.g. D^0 , τ) give moderately larger values, and random background combinations result in the largest values.

Transverse momentum ($\log(p_T)$): This variable is the transverse momentum of the additional signal particle with respect to the beam axis. Signal particles originating from b -hadron decays are typically produced in hard-scattering processes and therefore exhibit higher p_T compared to background particles arising from soft QCD interactions at the PV. It is particularly effective at distinguishing particles from excited states, such as kaons from $B_{s2}^*(5840) \rightarrow B^+ K^-$ decays, from those produced directly at the PV. While this feature introduces some dependence on the signal decay kinematics, its moderate discriminating power warrants its inclusion in the training.

Primary vertex displacement (*PV signed distance*): We define the signed displacement between the refitted candidate's decay vertex and its associated primary vertex (PV) as

$$\Delta \vec{r}_{\text{PV}} \equiv \vec{r}_{\text{SV}}^{\text{base+trk}} - \vec{r}_{\text{PV}}, \quad d_{\text{PV}}^{\text{signed}} \equiv \text{sign}(\Delta r_{\text{PV},z}) |\Delta \vec{r}_{\text{PV}}|.$$

Here, $\vec{r}_{\text{SV}}^{\text{base+trk}}$ is the decay vertex obtained after refitting the base candidate with the additional track, and \vec{r}_{PV} is the position of the *best PV* associated³ associated to it. $\Delta r_{\text{PV},z}$ denotes the z -component of the SV–PV displacement. For genuine long-lived decays (signal), the SV lies downstream of the PV, so $\Delta r_{\text{PV},z} > 0$ and $d_{\text{PV}}^{\text{signed}}$ is predominantly positive, with a positive tail set by the boosted flight distance. For background candidates formed by combining a genuine base candidate from the signal decay with a *prompt* PV track, the refit shifts the SV toward the prompt track's PV. Two common outcomes follow: (i) if the refitted SV is pulled *upstream* while the best-PV association remains *downstream*, then $z_{\text{SV}}^{\text{base+trk}} < z_{\text{PV}}^{\text{best}}$ and $d_{\text{PV}}^{\text{signed}}$

³The best PV is chosen as the primary vertex that minimises the candidate's impact-parameter (IP) with respect to the refitted candidate momentum.

becomes strongly negative, producing the pronounced negative tail; (ii) if the best PV *flips upstream* (often the prompt track’s PV), the SV sits close to that PV and $d_{\text{PV}}^{\text{signed}}$ populates the near-zero (or small positive) region. In dense multi-PV environments (e.g. Run 3), PV–PV separations enhance these effects: the mismatch between the SV pull and the best-PV choice can span several millimetres along z , naturally yielding very negative values.

Momentum angular separation (*Transformed* $\cos\theta$): This variable is the cosine of the opening angle θ between the combined momentum vectors of the base and additional particle. Signal particles, being part of the same decay, are expected to yield small opening angles (large $\cos\theta$ values). Background particles, especially from the PV or the other b -hadron, are less aligned. The transformation $1 - (1 - \cos\theta)^{0.2}$ enhances sensitivity in the region where signal and background overlap.

The distributions of the input features for signal and background particles are shown in Fig. 5, with the corresponding correlation matrix provided in Appendix C. An anti-correlation is observed between the *Transformed* ΔR and *Transformed* $\cos\theta$ variables for both signal and background categories, along with a moderate correlation between $\log(\chi_{\text{IP wrt SV}}^2)$ and $\log(\chi_{\text{DOCA}}^2)$. Apart from these, the features exhibit only weak correlations, suggesting that they offer largely complementary information for the classification task. The relative importance of each feature is discussed in the following section.

3.4 Training and performance

On average, each simulated decay “cocktail” contains $(3\text{--}4) \times 10^4$ *non-isolated* signal particles, accompanied by a substantially larger number of *isolated* background particles – typically 50 to 100 times more numerous than the signal. To train the IMI classifier, each cocktail is split into three statistically independent subsets: 70% for training, 15% for validation, and 15% for evaluation. During training and validation, the background class is *randomly down-sampled* to match the number of signal particles, enforcing a balanced class ratio that stabilises gradient updates. In contrast, the evaluation set retains the full class imbalance ($\gtrsim 50:1$), thus providing a realistic performance estimate under Run 3-like conditions at LHCb.

The classifier performance of IMI is quantified by the area under the receiver-operating-characteristic (ROC) curve, abbreviated AUC. Hyperparameters, including the number of trees n , maximum tree depth d , and learning rate λ , are tuned using the Bayesian optimisation framework OPTUNA [37]. The objective is to minimise the Kolmogorov-Smirnov (KS) statistic between the classifier outputs on the training and validation sets, thereby suppressing overfitting.

The IMI output for non-isolated (signal) and isolated (background) particles is shown in Fig. 6. The filled histograms represent the training sample, while the markers indicate the evaluation sample. The close agreement between the two confirms that the model generalises well and exhibits no signs of overtraining. Quantitatively, the classifier achieves an AUC of

$$\text{AUC} = 0.9964(3)$$

on the evaluation set, where the uncertainty reflects the variation across a thousand bootstrap replicas.

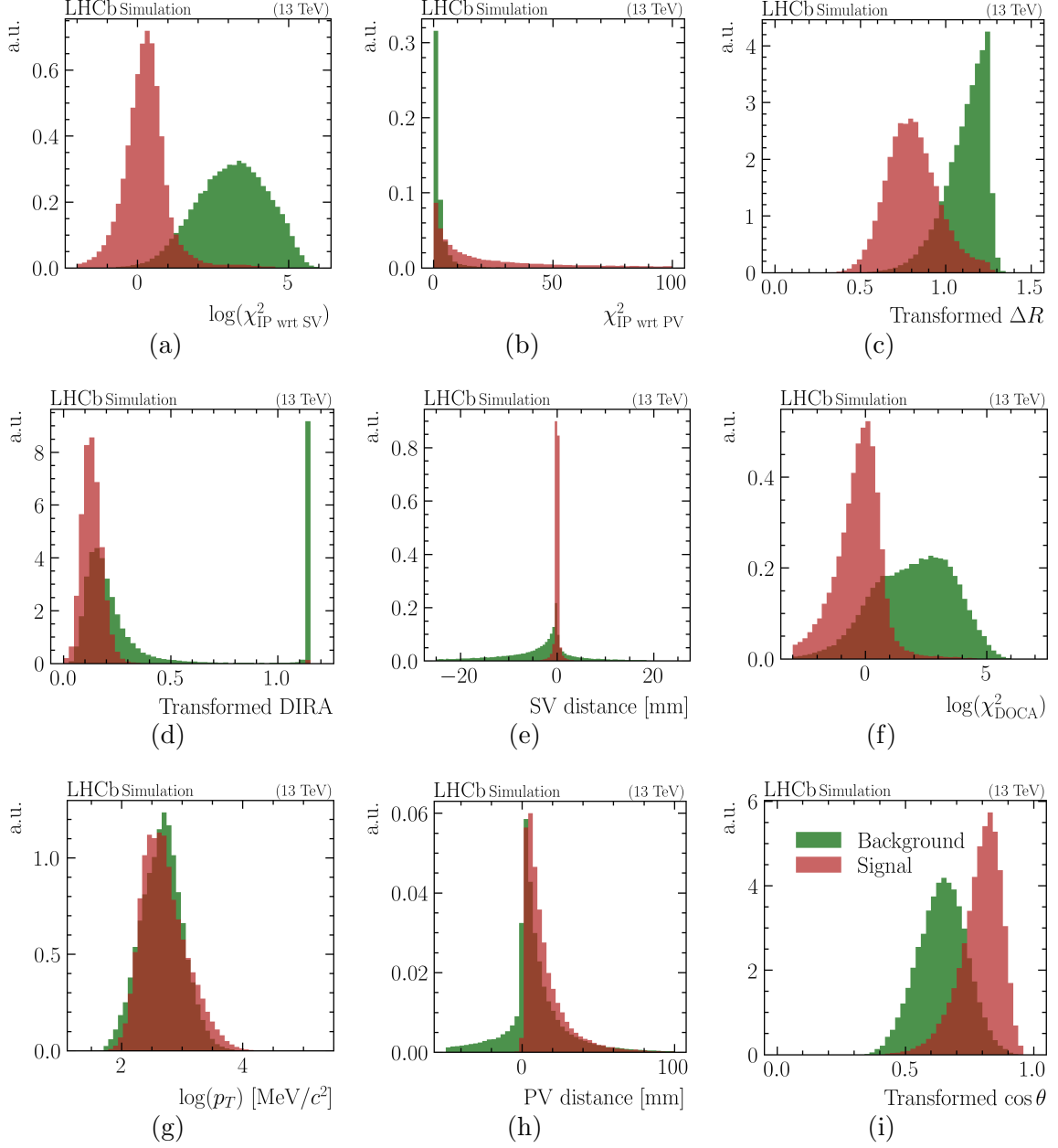


Figure 5: Distributions of the input features used to train the IMI. The curves for signal particles (non-isolated particles) are shown as red histograms, while background particles (isolated particles) are represented by green histograms. These variables serve as inputs to the multivariate classifier. See Sec. 3.3 for a detailed description of each feature.

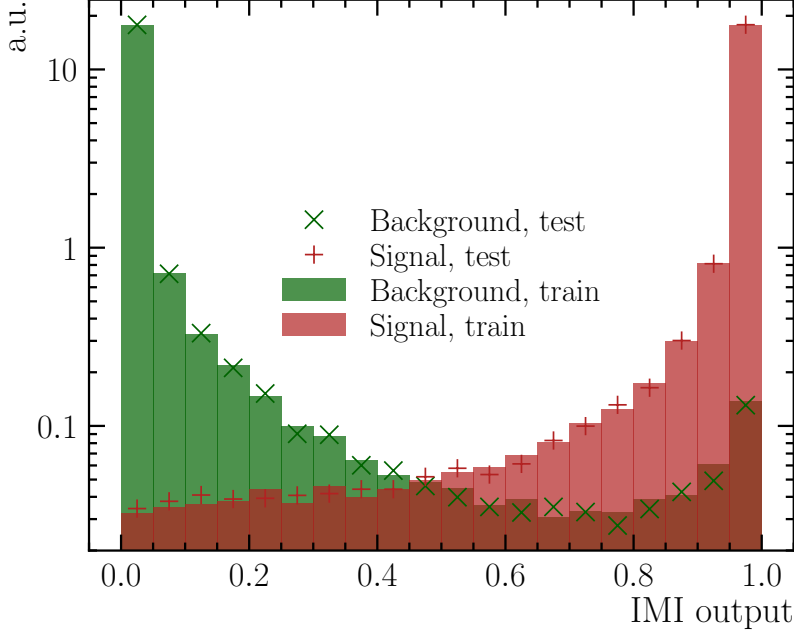


Figure 6: Distributions of the IMI classifier output for non-isolated signal (red) and isolated background (green) particles in the training sample (filled histograms) and evaluation sample (markers). The strong agreement confirms the absence of overtraining and the model’s ability to generalise to unseen data.

To elucidate the classifier’s internal logic, we compute SHAP (SHapley Additive exPlanations) values [38], which quantify the contribution of each feature to the model output on a per-particle basis. The summary plot in Fig. 7 orders the inputs by their mean impact and visualises their effects across the evaluation sample. Three variables clearly dominate the decision boundary: $\log(\chi^2_{\text{IP wrt SV}})$, $\chi^2_{\text{IP wrt PV}}$, and ΔR . Particles with *small* values of $\log(\chi^2_{\text{IP wrt SV}})$ or ΔR (green points) push the SHAP value toward positive numbers, yielding a signal-like prediction, whereas *large* values (red points) shift the output toward background-like. Conversely, a large $\chi^2_{\text{IP wrt PV}}$ indicates significant displacement from the primary vertex and therefore increases the signal score, while small values suppress it, complementary behaviour to the other two variables. Secondary inputs, including the *Transformed DIRA*, *SV distance*, and $\log(\chi^2_{\text{DOCA}})$, introduce fine-grained topological information that sharpens the separation between classes. Kinematic observables such as $\log p_T$ play a supportive, albeit less critical, role. The narrow SHAP ranges observed for *PV distance* and the *Transformed cos θ* demonstrate that the model does not over-rely on weakly informative features. Overall, the SHAP analysis confirms that the classifier’s decisions are governed by physically meaningful observables and remain fully aligned with the underlying isolation logic.

The benchmarking of the IMI tool against classical isolation methods is provided in Sec. 3.4.1, while its performance as a function of event multiplicity is discussed in Sec. 3.4.2. The dependence of signal efficiency on key kinematic variables is examined in Sec. 3.4.3.

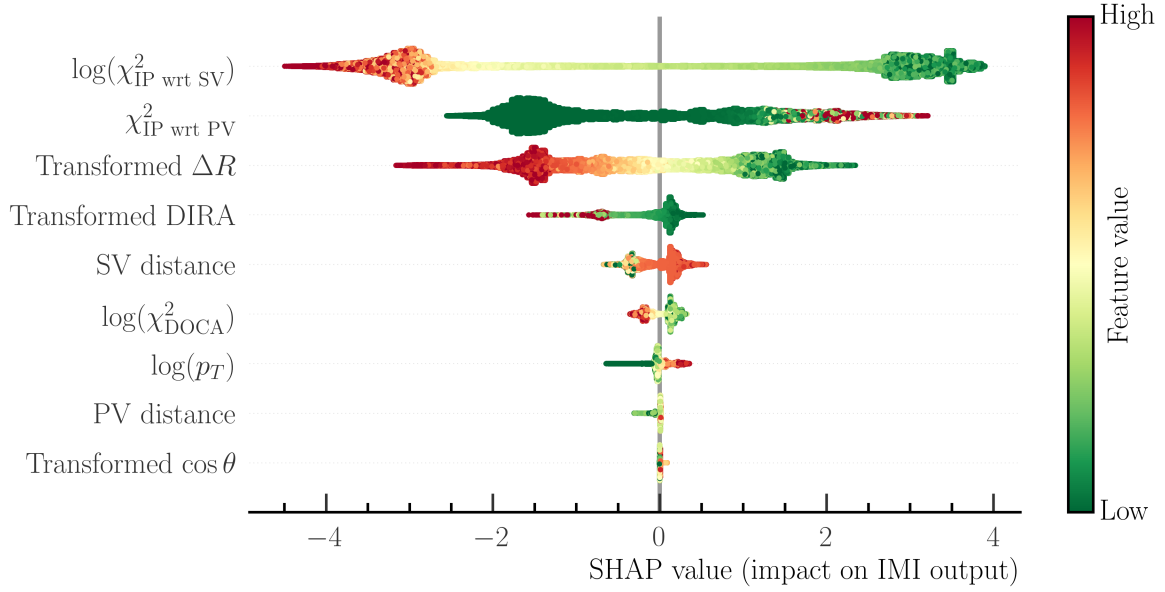


Figure 7: SHAP summary plot for the IMI classifier [38]. The y-axis lists input features in order of decreasing importance. The x-axis indicates each feature’s SHAP value, that is, its contribution to the classifier’s output, while the color encodes the raw feature value (green = low, red = high). Positive SHAP values push the classifier toward signal-like predictions, while negative values indicate background-like behavior.

3.4.1 Comparison with Classical Isolation

The performance of the IMI tool is benchmarked against classical isolation techniques described in Sec. 2, namely, the *track isolation* and *cone isolation* methods. Figure 8 shows the ROC curves obtained from the inclusive simulated samples listed in Table 1. In these plots we evaluate the signal *candidate* efficiency rather than the signal *track* efficiency, since candidate-level efficiencies are lower and more directly relevant for physics analyses that reconstruct full decay chains. By contrast, the background rejection is defined with respect to background *tracks*, as these particles do not form part of any reconstructed candidate. The results demonstrate that IMI provides the best overall performance, reaching about 99 % background rejection at 95 % signal *candidate* efficiency. Beyond this point, the curve drops steeply, indicating a sharp and well-defined operational threshold. The *cone isolation* method, which accepts extra particles within a maximum angular separation $\Delta R < x$ from the base particle, can approach similar maximum background rejection, but only in a much narrower efficiency range ($\varepsilon_{\text{sig}} \approx 0\text{--}50\%$). This reflects a key limitation of relying solely on geometric separation: particles from the dense underlying event can mimic the topology of genuine signal tracks, reducing discrimination power at higher efficiencies. The *track isolation* method, based on requiring either the `samePV` association with the base particle or $\chi^2_{\text{IP wrt PV}} > y$, is constrained by the binary nature of the `samePV` selection. Once most background particles are assigned to the correct primary vertex, its rejection power saturates at about 70 %, and performance degrades quickly for $\varepsilon_{\text{sig}} \gtrsim 95\%$. Overall, the results highlight that IMI leverages a richer set of features beyond pure geometry or vertex association, enabling it to maintain both high background

rejection and high signal efficiency over a wide operating range. The signal efficiency and background rejection power for all three methods as function of the threshold values is shown in the Appendix D.

The lower panels of Fig. 8 explore performance of track (left), cone (middle), and IMI (right) isolation methods applied to three exclusive decay channels with varying kinematics and numbers of non-isolated signal particles (see Table 1):

- $B^0 \rightarrow D^{*-}\mu^+\nu_\mu$, featuring one non-isolated signal particle with soft kinematics;
- $\Lambda_b \rightarrow \Lambda_c^{+*}\mu^-\bar{\nu}_\mu$, featuring two relatively hard non-isolated signal particles;
- $B_s^0 \rightarrow D_s^{(*)-}\ell^+\nu_\ell$, with two to five non-isolated particles, including children of a long-lived D_s^- .

Across all three benchmark channels, IMI maintains a robust and consistent performance, demonstrating that it is agnostic to the number of non-isolated signal particles. In contrast, the *track isolation* method shows similarly modest performance for each decay, underscoring that its discriminating power is governed almost entirely by the $\chi_{\text{IP wrt PV}}^2$ threshold. Minor variations in signal efficiency stem from correlations between particle kinematics and impact parameter significance. *Cone isolation*, however, exhibits strong sensitivity to the decay topology. In the $B^0 \rightarrow D^{*-}\mu^+\nu_\mu$ decay, where the base and signal particles are well collimated, its performance is relatively good. But in decays with more or softer non-isolated particles, such as $D_s^{(*)-}$ or $\Lambda_c^{(*)}$ modes, the performance declines sharply. This is because a larger cone size is needed to include all signal particles, inadvertently admitting more background.

The IMI working point is intentionally set to a conservative response threshold of 0.05. At this setting, the number of selected signal particles per event is reduced from the $\mathcal{O}(200)$ charged particles typically reconstructed to about $\mathcal{O}(10)$, while retaining a signal efficiency of roughly 99 %. Although exclusive trainings generally outperform the inclusive ones, as they are optimised for a specific signal topology and kinematics, the low threshold ensures that a broad set of signal-like particles is retained. This allows analysts to perform more specialised trainings at the analysis stage while still benefiting from strong background rejection.

3.4.2 Performance as a function of event multiplicity

We evaluate the robustness of different isolation methods in increasingly busy events by studying their performance as a function of event multiplicity, defined as the number of reconstructed charged particles in the event. This variable serves as a proxy for overall event activity, which is particularly relevant in hadronic collisions where occupancy can vary substantially. Each method is benchmarked at a fixed signal efficiency of approximately 99 %, and its background rejection power is assessed across the multiplicity spectrum.

Figure 9 compares three isolation strategies, *track isolation*, *cone isolation*, and IMI, as a function of event multiplicity, using the simulation cocktail sample described in Table 1. Across the full range of event multiplicities, the IMI algorithm demonstrates a clear advantage, consistently rejecting around 95 % of background while retaining 99 % signal efficiency. The *track isolation* method shows steadily improving performance with increasing multiplicity, reaching up to 50 % background rejection in high-occupancy events. This improvement arises because the isolation requirement is particularly effective at

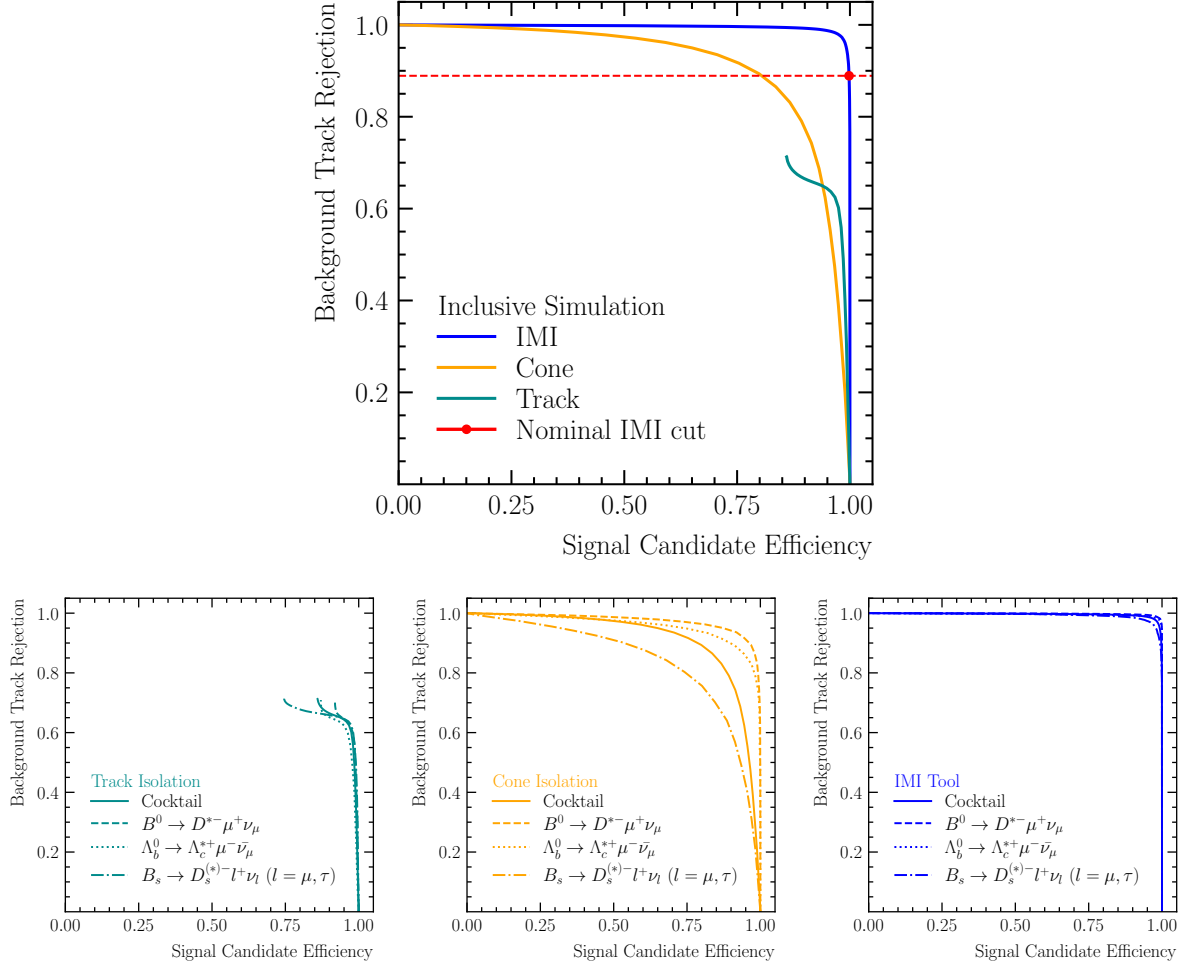


Figure 8: Signal *candidate* efficiency versus background *track* rejection for the Track (cyan), Cone (orange), and IMI (blue) isolation methods. The top panel shows performance on the inclusive MC cocktail sample. The bottom panels show the performance of each method, Track (bottom-left), Cone (bottom-middle), and IMI (bottom-right), applied to exclusive decay channels with increasing numbers of non-isolated signal particles (see Table 1): $B^0 \rightarrow D^{*-}\mu^+\nu_\mu$ (1 non-isolated particle), $\Lambda_b \rightarrow \Lambda_c^{*+}\mu^-\bar{\nu}_\mu$ (2 non-isolated particles), and $B_s^0 \rightarrow D_s^{(*)-}\ell^+\nu_\ell$ (2 to 5 non-isolated particles), where $\ell \in \{\mu^\pm, \tau^\pm\}$. The red marker in the top panel indicates the chosen IMI working point.

rejecting tracks originating from primary vertices other than the one that produced the signal candidate. In contrast, the *cone isolation* method yields relatively flat performance, plateauing at around 20 % background rejection. Its effectiveness is significantly lower than the other methods, especially in high-multiplicity environments where the isolation cone is more likely to contain unrelated particles.

The lower panels of Fig. 9 present the same comparison for three exclusive benchmark channels, introduced earlier, that differ in kinematics and in the number of non-isolated particles: $B^0 \rightarrow D^{*-}\mu^+\nu_\mu$ (one soft), $\Lambda_b \rightarrow \Lambda_c^{*+}\mu^-\bar{\nu}_\mu$ (two relatively hard), and $B_s^0 \rightarrow D_s^{(*)-}\ell^+\nu_\ell$ (two to five, including daughters of a long-lived D_s^-). Across all three channels, IMI achieves the best performance, delivering 90–95 % background rejection while maintaining 99 % signal efficiency. The *track isolation* method performs similarly for the B^0 and B_s^0

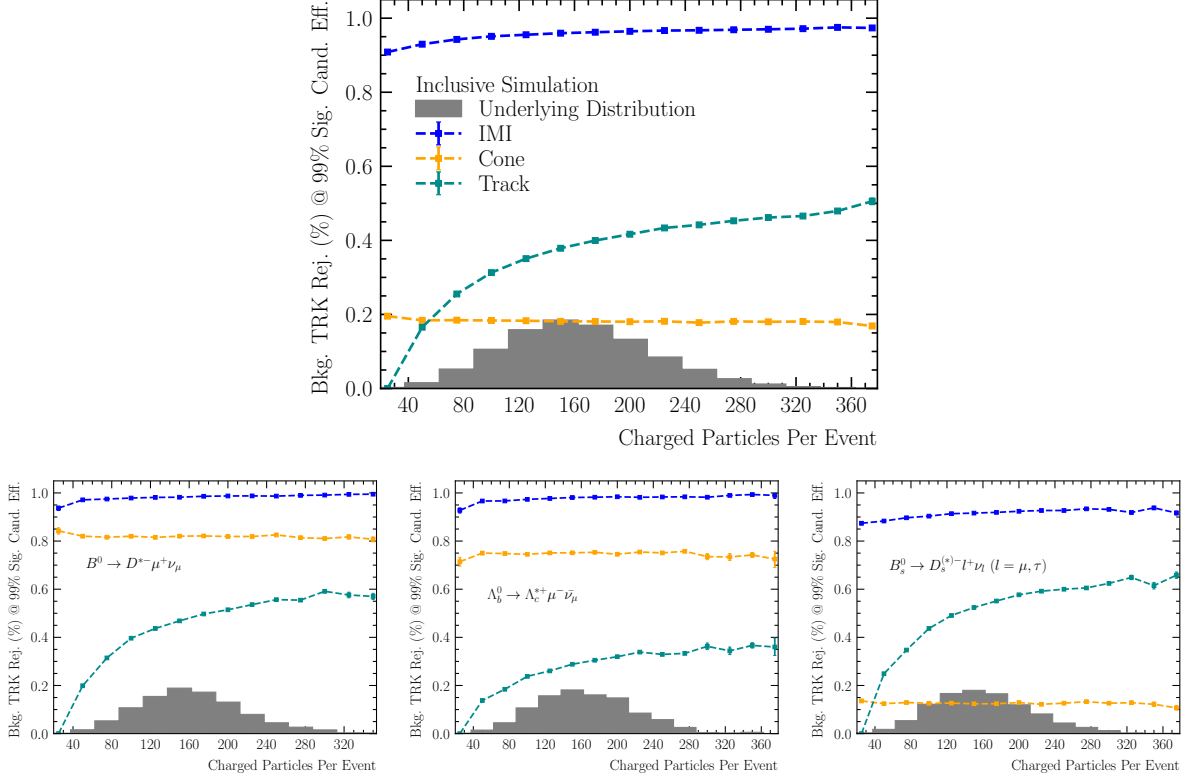


Figure 9: Background rejection at a fixed signal efficiency of approximately 99% for the Track (cyan), Cone (orange), and IMI (blue) isolation methods as a function of number of charged particles in the event (event multiplicity). The top panel shows performance on the inclusive simulated cocktail sample (see Table 1). The bottom panels show the performance for three exclusive decay channels with varying kinematics and numbers of non-isolated signal particles: $B^0 \rightarrow D^{*-} \mu^+ \nu_\mu$ (1 non-isolated particle, left), $\Lambda_b^0 \rightarrow \Lambda_c^{*+} \mu^- \bar{\nu}_\mu$ (2 non-isolated particles, middle), and $B_s^0 \rightarrow D_s^{(*)-} \ell^+ \nu_\ell$ (2 to 5 non-isolated particles, right), where $\ell \in \{\mu^\pm, \tau^\pm\}$. The IMI tool consistently outperforms the classical methods across all event multiplicities and decay channels.

decays, but slightly worse for the Λ_b decay. This difference arises because the relatively soft non-isolated particles in B^0 and B_s^0 decays tend to have larger impact parameters with respect to the PV than the harder particles from Λ_b decays, settling on a minimal $\chi_{\text{IP wrt PV}}^2$ requirement that is more effective at rejecting background in the former cases. In contrast, the *cone isolation* method gives comparable results for the B^0 and Λ_b decays, but performs significantly worse for the B_s^0 decay. For B_s^0 decays, reconstructing signal particles from long-lived D_s^- mesons requires a larger isolation cone, which inevitably captures more background and reduces rejection power.

3.4.3 Signal efficiency as a function of kinematic variables

We also assess whether the signal efficiency of each isolation method varies as a function of key kinematic variables, particularly the squared four-momentum transfer, $q^2 = (p_B - p_{\text{had}})^2$, which is equivalently the invariant mass squared of the lepton–neutrino system (e.g. $q^2 = m_{\ell\nu_\ell}^2$ for $B^0 \rightarrow D^{*-} \ell^+ \nu_\ell$ decays). Ideally, a well-designed selection should yield a flat efficiency across the entire q^2 spectrum. This is especially important at high

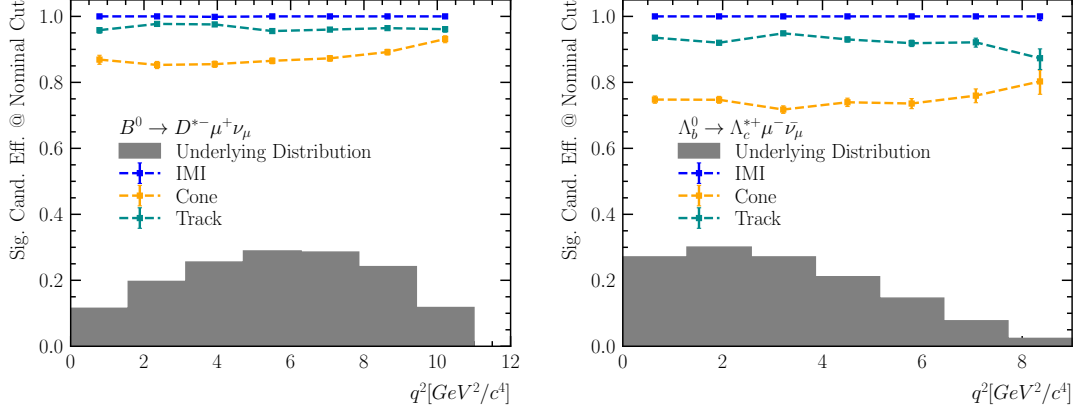


Figure 10: Signal efficiency as a function of q^2 for different isolation methods: IMI with output > 0.05 (blue), *track isolation* with `samePV` and $\chi^2_{\text{IP wrt PV}} > 16$ (cyan), and *cone isolation* with a fixed cone size of 0.5 (orange). Shown are two decay channels: $B^+ \rightarrow D^{*-} \mu^+ \nu_\mu$ (left), with one non-isolated signal particle, and $\Lambda_b \rightarrow \Lambda_c^{*+} \mu^- \bar{\nu}_\mu$ (right), with two. Here Λ_c^* represents $\Lambda_c(2625)$ state.

q^2 , where theoretical predictions from lattice QCD are most precise, enabling precision measurements of CKM matrix elements.

To study this, we evaluate the signal efficiency as a function of q^2 for each isolation method. For the IMI tool, we apply the nominal working point defined earlier, corresponding to a IMI output threshold of $\text{IMI} > 0.05$ on each signal particle. For *track isolation*, we use the `samePV` flag or $\chi^2_{\text{IP wrt PV}} > 16$. For *cone isolation*, we use a fixed cone size of $\Delta R = 0.5$ which is typically used to capture the b -jet structure. Figure 10 shows the resulting signal efficiencies for two representative decay channels: $B^+ \rightarrow D^{*-} \mu^+ \nu_\mu$ (left), with one non-isolated signal particle, and $\Lambda_b \rightarrow \Lambda_c^{*+} \mu^- \bar{\nu}_\mu$ (right), with two non-isolated particles where Λ_c^* denotes $\Lambda_c(2625)$ state. While the *cone isolation* and *track isolation* exhibit modest efficiency variations, largely reflecting their unavoidable correlation with the signal particle kinematics, the IMI tool, in contrast, preserves a consistently high and nearly flat efficiency across the entire q^2 range.

4 Implementation and data size reduction

This section describes the implementation of both classical and the new IMI isolation algorithms, and their integration into the LHCb software framework in sub-section 4.1. The data size reduction achieved by the IMI and its impact on SPRUCING throughput are discussed in Sub-section 4.2.

4.1 Integration into the LHCb selection framework

The computation of classical isolation variables, introduced in Section 2, is implemented in the LHCb software through two complementary workflows, illustrated in Figure 11.

Classical isolation A: In this implementation, combinations are formed between the reconstructed base particles and all other charged particles in the event that could

contribute to the isolation assessment. The selected additional particles are persisted for offline use, where cone- and vertex-based observables are computed by explicitly fitting a vertex between the base and each extra particle. These observables can then be stored [39] and used directly in offline analyses. The corresponding algorithms are implemented within the REC reconstruction framework [40].

Classical isolation B: The second implementation follows the same principle as the first, but computes the isolation variables directly at the trigger level. Instead of persisting the full information of the additional particles, only a minimal set of observables is stored, which significantly reduces the average event size. To optimise throughput in the case of vertex isolation, no dedicated vertex fit is performed; rather, the observables are derived from the impact-parameter significance of the extra particles with respect to the vertex formed by the base particles. This approach is well motivated, since the impact-parameter χ^2 with respect to the decay vertex and the change in the vertex-fit χ^2 when adding the extra track are found to be equivalent. The resulting quantities are written to the event record and can be used directly in offline analyses. The corresponding algorithm is implemented within the REC reconstruction framework [40].

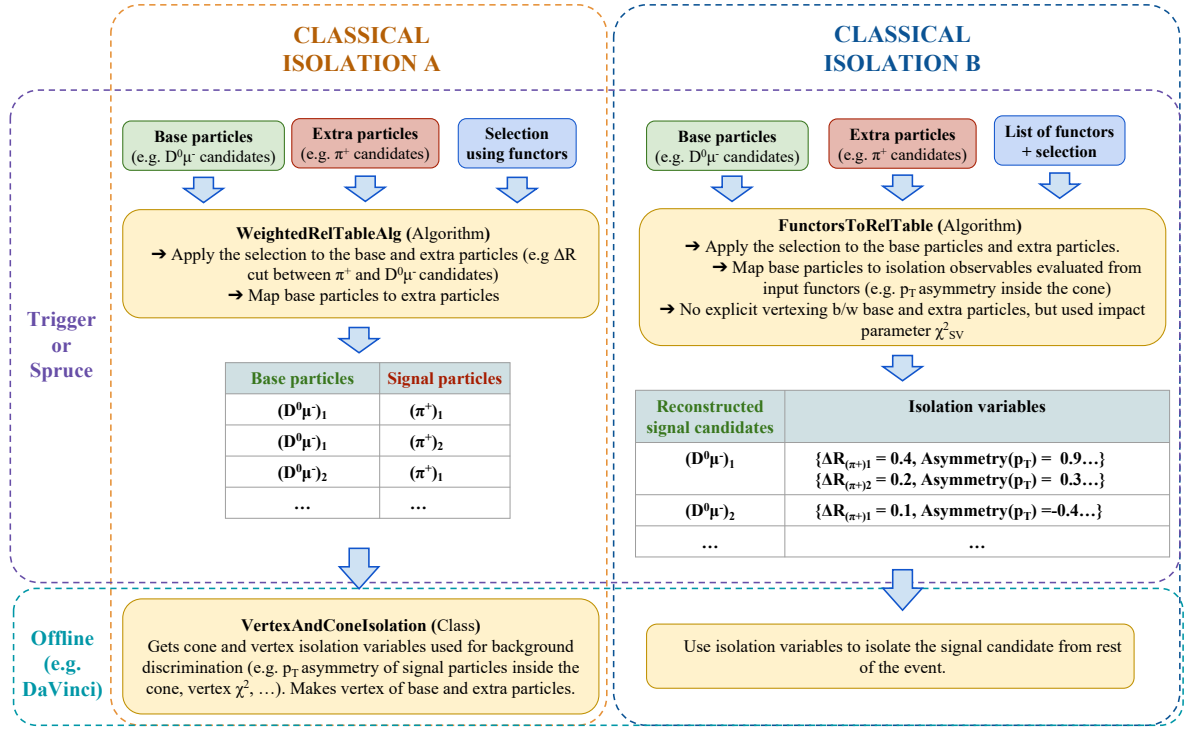


Figure 11: Comparison of the two classical isolation strategies implemented in the LHCb selection framework. Although type “B” is designed for the trigger, it can also be run offline, ensuring consistent isolation variable computation across channels using different strategies.

Inclusive multivariate isolation: The IMI strategy follows a conservative data-storage model. At the trigger level, all reconstructed particles in the event are written to tape, and the actual isolation decision is deferred to the SPRUCING stage, where the fully

reconstructed event is available. At this point, only those additional particles identified as signal-like are retained on disk, leading to a significant reduction in event size. As illustrated in Fig. 12, each signal candidate is combined with every other particle in the event, and a vertex fit is attempted. To avoid an excessive number of combinations, loose fiducial cuts are applied to the additional particles, such as $\log(\chi^2_{\text{IP w.r.t. SV}}) < 5$, a minimum PV distance greater than -3 mm, and a minimum SV distance greater than -5 mm. A multivariate classifier then evaluates each base-extra particle pair and assigns an IMI score. The resulting relation table, linking base particles to additional particles with their IMI scores, provides a flexible input for offline analyses. It can be used to suppress backgrounds, to rank extra particles when reconstructing complex decay chains, or to define background-enriched control regions. Again all the related algorithms form part of the REC project [40].

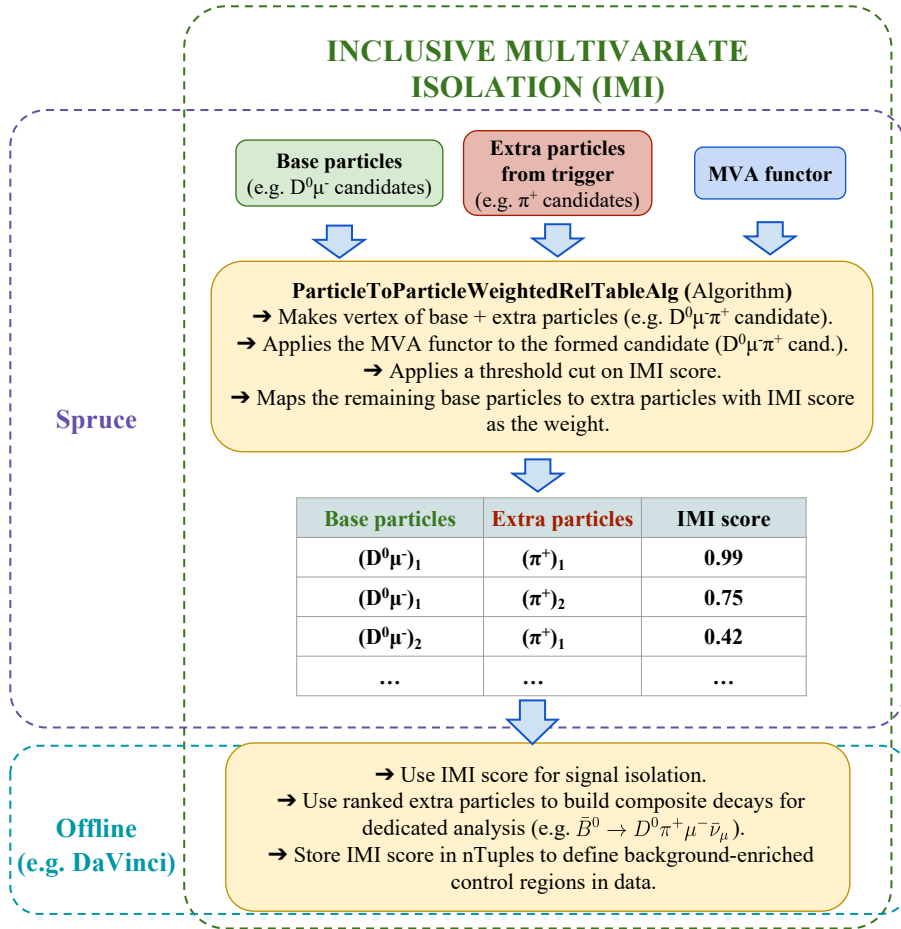


Figure 12: Isolation workflow based on the Inclusive Multivariate Isolation (IMI) approach.

4.2 Data-size reduction and throughput

Before integrating the IMI algorithm into the LHCb selection framework, it was essential to demonstrate that it could deliver a substantial reduction in the volume of data written to disk, *without* compromising on the processing throughput. To evaluate this trade-off,

we processed a large sample of minimum-bias simulation events generated under Run 3 conditions, with all semileptonic SPRUCING selection lines enabled. These lines typically reconstruct on average two b -hadron candidates and write minimal information to disk.

For each combination of a base particle and an extra particle in the event, the maximum IMI score is evaluated, and the combination is retained only if this score exceeds a configurable threshold. By scanning the threshold from 0 to 1 in steps of 0.01, we map out the relationship between (i) the relative reduction in output file size, (ii) changes in processing throughput, and (iii) the signal-candidate efficiency. The results are presented in Fig. 13. The left panel shows the relative file-size reduction (blue) and throughput variation (red). The filesize measurement is normalised to the baseline where no cut is applied (i.e., all additional particles are retained) and throughput is normalised relative to if all particles are saved without running the IMI at all. The right panel shows the direct trade-off between file-size reduction and signal-candidate efficiency, where the signal efficiency is the one obtained using the simulation cocktail (Table 1).

At the nominal working point, defined by $\text{IMI} > 0.05$, the output file size is reduced by 45%, while preserving more than 99% of signal candidates. It is worth noting that the maximum achievable file-size reduction asymptotes at roughly 50%, as the remaining portion consists of indispensable reconstructed content such as primary vertices, base particles, neutral objects, and trigger information (see Fig. 1). Crucially, the throughput remains essentially constant, increasing by less than 0.1%, across the full threshold range. This is to be expected as all combinations of base particles and additional charged particles will be made regardless of the chosen cut value. The slight increase in throughput at higher thresholds simply reflects fewer events being written, which is a comparatively light computational task.

Although IMI is intrinsically lightweight at the inference stage, its integration introduced overheads from vertex fitting, resulting in a throughput reduction of around 20% in SPRUCING. This defines the scale of the reduction shown in Fig. 13 (left). Such an overhead is acceptable at SPRUCING, where throughput is far less critical than in Hlt2. For example, the FULL stream in Hlt2 operates at input rates of 0.5–1.5, MHz, while SPRUCING handles only about 0.04, MHz – over a factor of thirty lower. In this context, the modest throughput penalty at SPRUCING is clearly outweighed by the $\sim 45\%$ reduction in file size, which significantly improves downstream data handling and storage efficiency.

5 Validation in data

While classical isolation algorithms from Run 2 have been successfully adapted and re-designed for Run 3, the IMI algorithm represents a completely new development. Given that much of the current semileptonic physics programme at LHCb, particularly analyses involving excited charm (and charmless) states and so-called “double-charm” decays, relies heavily on this algorithm, a robust validation in data is essential.

5.1 Ranking behaviour in real data

The IMI algorithm assigns a score to each extra particle near a selected signal candidate, reflecting the likelihood that it originates from the same decay chain as the base particle.

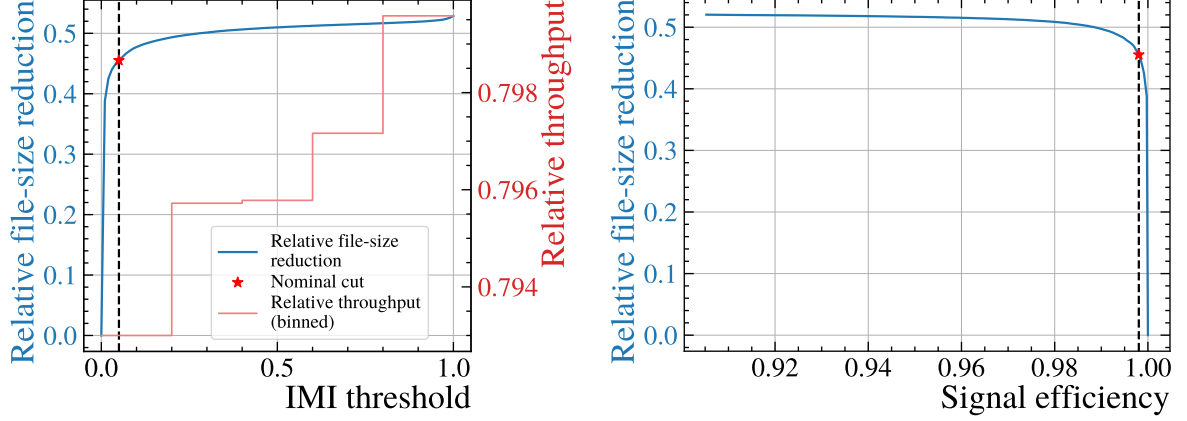


Figure 13: (Left) Relative reduction in output file size (blue) and inference throughput (red) as a function of the IMI threshold. Throughput is evaluated in 0.01 steps and summarised as the median in bins of width 0.2. The throughput is measured across all production LHCb sprucing lines relative to if isolation was ignored entirely and rather everything were blindly saved. Throughput is also noted to be roughly independent of the IMI threshold as all candidates combinations are made independent of this cut. Since this occurs at the SPRUCING stage, where throughput is not critical, the overhead is acceptable given the nearly 45% reduction in file size. (Right) File-size reduction versus signal-candidate efficiency on the simulation cocktail. The nominal working point is indicated by the vertical dashed line and red maker at IMI = 0.05.

To verify that this ranking is physically meaningful, we compare features of the highest-, second-highest-, and lowest-ranked extra particles using partial Run 3 data used to reconstruct $B^0 \rightarrow D^{*-} \ell^+ \nu_\ell$ candidates. Figure 14 shows the distributions of two key input features: cone angle (ΔR) and IP χ^2 with respect to the SV, $\log(\chi_{\text{IP wrt SV}}^2)$. As expected, the highest-ranked particles cluster in the region of small ΔR and low χ_{IP}^2 , indicating that they are likely to originate from the same decay chain as the base particle.

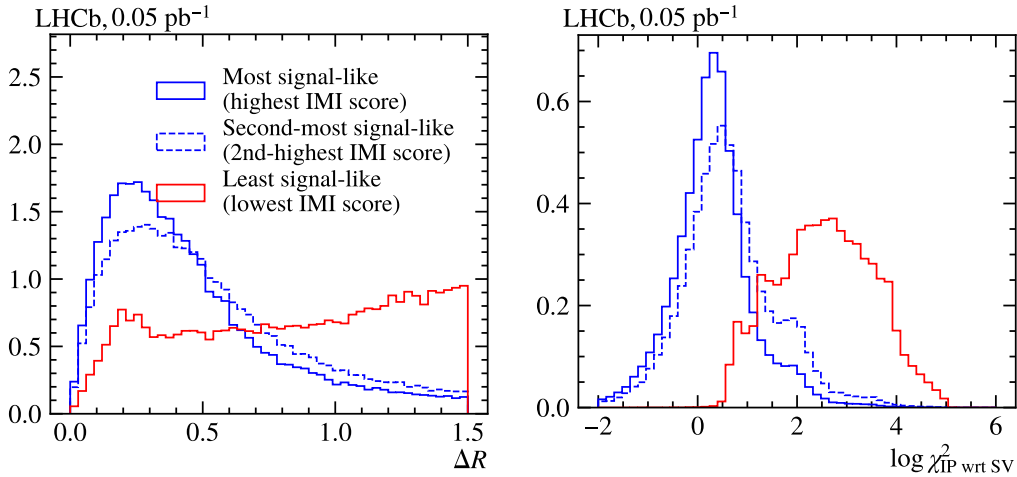


Figure 14: Distributions of (left) ΔR and (right) $\log(\chi_{\text{IP wrt SV}}^2)$ for $B^0 \rightarrow D^{*-} \ell^+ \nu_\ell$ candidates, split by the IMI ranking of the extra particle.

5.2 Reconstructing resonances using IMI-selected particles

A more stringent test of the algorithm’s performance is whether the extra particles selected by IMI can be used to reconstruct well-known resonances, without relying on channel-specific tuning.

We first consider reconstruction of the $D^{*-} \rightarrow \bar{D}^0 \pi^-$ decay. Starting from a clean $\bar{D}^0 \rightarrow K^+ \pi^-$ candidate, we combine the single highest-ranked extra particle with negative charge (assumed to be a π^-) with the base particles to form a D^{*-} . The resulting $\Delta M_{D^{*-}} \equiv |M_{D^{*-}} - M_{\bar{D}^0}|$ spectrum, shown in Fig. 15 (top), exhibits a clear, narrow peak on top of a small combinatorial background. Notably, only loose particle identification requirements are applied to the base particles, further highlighting the discriminating power of IMI.

A similar validation is performed in $\Lambda_b^0 \rightarrow \Lambda_c^{*+} \mu^- \bar{\nu}_\mu$ decays, where excited charm baryons $\Lambda_c^{*+} \rightarrow \Lambda_c^+ \pi^+ \pi^-$ are reconstructed by combining the two highest-ranked oppositely charged extra particles with a Λ_c^+ baryon. The resulting $\Delta M_{\Lambda_c^*} = M(\Lambda_c^+ \pi^+ \pi^-) - M(\Lambda_c) - M_{PDG}(\Lambda_c)$ distribution, shown in Fig. 15 (bottom), reveals peaks corresponding to the $\Lambda_c(2595)^+$ and $\Lambda_c(2625)^+$ resonances, as well as a structure around the $\Lambda_c(2880)^+$. Again, these results are obtained with minimal selection, demonstrating that IMI can reliably recover non-isolated signal decay products in data.

5.3 Isolation efficiency in data and simulation

While the IMI algorithm performs well qualitatively, it is also important to evaluate its signal efficiency quantitatively, and compare data to simulation. Figure 16 shows the efficiency of the IMI selection (left) and the fraction of charged particles accepted per event (right), as a function of the threshold, computed on simulated $B^0 \rightarrow D^{*-} \ell^+ \nu_\ell$ events and compared to background-subtracted partial Run 3 data that reconstructs the same decay. At low thresholds, the agreement between data and simulation is excellent. However, at tighter IMI thresholds the efficiency begins to diverge. This indicates some mismodelling of the input-feature distributions in simulation, which could be mitigated by applying inclusive simulation-to-data corrections in the future. Nevertheless, by operating with very loose IMI cuts, chosen to retain high signal efficiency, we ensure that these discrepancies have minimal impact on downstream physics analyses.

6 Summary and Outlook

For Run 3, the LHCb experiment faces the demanding task of reducing data rates by up to a factor of eight, imposing stringent constraints not only on which events are selected, but also on the size of each recorded event. While signal decays typically involve just 5–7 charged particles, a typical Run 3 event contains $\mathcal{O}(200)$ reconstructed tracks, with charged particle information alone accounting for over 50% of the total event size. To address this imbalance, a suite of inclusive isolation tools were developed, including classical track-, cone-, and vertex-based methods, alongside a new Inclusive Multivariate Isolation (IMI) algorithm.

As its name implies, IMI is inherently both inclusive in scope and multivariate in structure. It is inclusive in that it has been trained from a wide range of simulated events, encompassing diverse decay topologies and kinematic configurations, including scenarios

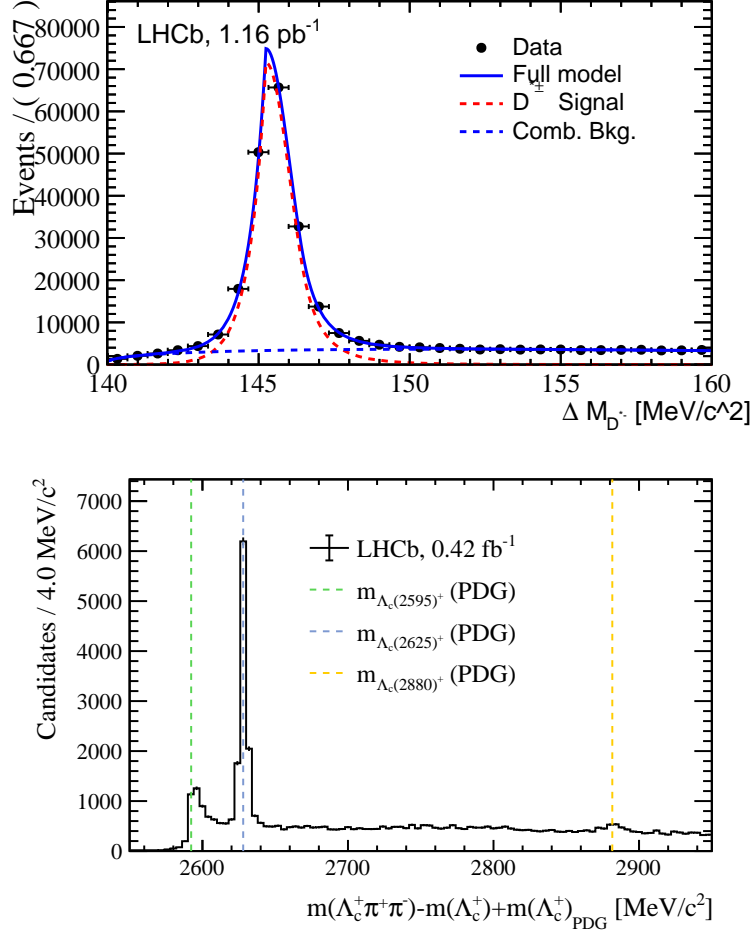


Figure 15: (Top) $\Delta M_{D^{*-}}$ distribution in partial Run 3 data, using the highest-ranked π^- to reconstruct D^{*-} mesons from \bar{D}^0 candidates. The signal (red) and background (dashed blue) fit components are overlaid. (Bottom) The $\Delta M_{\Lambda_c^{*+}} = M(\Lambda_c^{*+} \pi^+ \pi^-) - M(\Lambda_c^{*+}) - M_{PDG}(\Lambda_c^{*+})$ distribution in partial Run 3 data, using the two highest-ranked oppositely charged particles to reconstruct Λ_c^{*+} baryons from Λ_c^+ candidates. Vertical lines indicate the known Λ_c^{*+} masses from PDG.

where signal particles emerge from both short- and long-lived intermediate states within the b -hadron decay chain. Its multivariate nature arises from combining the prominent features of all classical isolation techniques – cone-, vertex-, and track-based – into a single classifier. Built on the fast and lightweight XGBoost framework, IMI assigns a score to each extra particle based on its compatibility with a signal origin, allowing only the most relevant particles to be retained for downstream analysis. This selective retention enables the efficient reconstruction of complex decay chains with varying final-state multiplicities and facilitates the definition of background-enriched control regions, both essential for controlling systematic uncertainties in precision measurements. As of 2025, IMI plays a central role in the LHCb semileptonic physics programme involving missing energy and is well suited for broader application to other decay channels.

The IMI algorithm delivers exceptional performance across a broad range of decay modes and event multiplicities, consistently outperforming classical isolation techniques. It achieves an area under the curve (AUC) of 0.997, demonstrating strong separation power

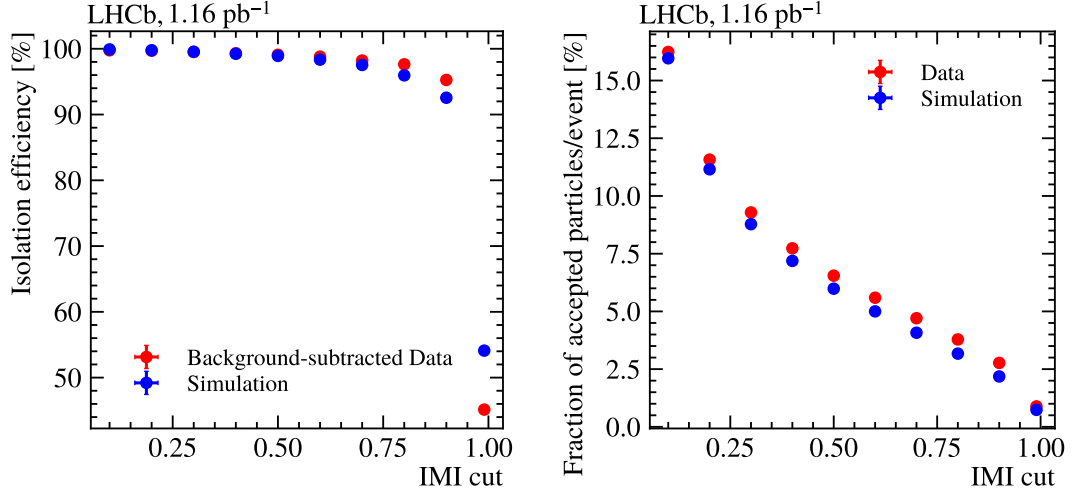


Figure 16: Signal efficiency (left) and fraction of charged particles accepted per event (right) as function of IMI threshold, computed on simulated $B^0 \rightarrow D^{*-} e^+ \nu_e$ events and compared to partial Run 3 data.

between signal and background particles. At its nominal working point, IMI rejects over 90% of background while retaining approximately 99% of signal particles, representing a $2\text{--}5\times$ improvement in background rejection relative to traditional methods in the inclusive sample. Crucially, this performance is preserved even in high-multiplicity environments and across diverse decay topologies, without introducing biases in sensitive kinematic observables such as the momentum transfer squared (q^2) in semileptonic decays. By retaining only $\mathcal{O}(10)$ signal-like particles out of the $\mathcal{O}(200)$ reconstructed tracks per event, IMI yields a significantly cleaner event representation, leading to a data size reduction of approximately 45%.

Both the classical and IMI isolation algorithms are fully integrated into the LHCb selection framework, each optimised for a different stage of the data-processing pipeline. The two also operate independently: selection lines using IMI do not rely on candidates preselected with the classical isolation tool. Classical isolation is deployed directly at the trigger level through two complementary approaches: one links signal particles to a minimal set of nearby tracks based on cone isolation, enabling isolation observables to be computed offline; the other computes and stores these observables at the trigger stage itself, allowing for immediate event size reduction with minimal impact on processing throughput. In contrast, IMI adopts a more conservative strategy: the full reconstructed event is written to tape after the trigger stage, and IMI is applied later at the offline SPRUCING stage, all while ensuring that the additional memory and throughput cost remains non-significant. This design offers long-term flexibility, as the SPRUCING stage can be re-run on triggered events, enabling future updates to IMI without the need to modify or reprocess data at the trigger level.

Validation using Run 3 data confirms that the IMI algorithm performs reliably under real data taking conditions. It produces physically consistent and interpretable rankings of extra particles in the event, enabling the reconstruction of well-known resonances such as the D^{*+} and Λ_c^* without requiring dedicated tuning. For the loose working point used in production, the agreement between data and simulation in terms of signal efficiency is

excellent across the phase space relevant to most analyses. These results demonstrate good confidence in the use of IMI as a core isolation tool in the LHCb selection framework.

In the near term, planned improvements to IMI include extending isolation to neutral particles (Fig. 1), adding VELO-based features for dense environments, and adopting a multiclass classifier to identify excited heavy-flavour states currently treated with cut-based selections (Appendix B). Looking further ahead, an attractive possibility is a broader architectural role for IMI as a fast pruning layer in multi-stage reconstruction. In this setup, IMI would ease the load on more complex, compute-intensive stages (e.g., GNN-based approaches [41]), helping to keep data volumes manageable in Run 4 and enabling the $\mathcal{O}(20)$ reductions anticipated for Run 5 [42, 43]. In conclusion, the demonstrated Run 3 performance and lightweight design make IMI a compelling and forward-compatible building block for scalable reconstruction in future runs.

Acknowledgements

We thank the *LHCb Simulation Project* for the support in producing the simulated samples used in this work. We are also grateful to the *Real-Time Analysis (RTA) Project* and *Data Processing and Analysis (DPA) Project* for their valuable contributions throughout the project. T. Fulghesu, C.-H. Li, A. Morris, and D. vom Bruch are supported by the European Research Council Starting Grant ALPACA (No. 101040710). A. Mathad and L. Hartman are supported by CERN. M. Calvi and V.S. Kirsebom are supported by Università di Milano-Bicocca, the Swiss National Science Foundation (SNSF, P500PT_222273), the Istituto Nazionale di Fisica Nucleare (INFN), and CERN. G. Hallett, T. Latham, M. Lehuraux, M. Monk, and F. Swystun are supported by the UK Science and Technology Facilities Council (STFC). M. Monk also acknowledges support from the Monash Warwick Alliance. M. Monk and F. Swystun acknowledge support from UK Research and Innovation under grant #EP/X014746/2. M. Rudolph is supported by the U.S. Department of Energy (DOE) and the National Science Foundation (NSF).

A Inclusive simulation samples

Table 1 provides an overview of the simulated b -hadron decay modes used to train the IMI algorithm. The samples cover a broad range of decay topologies, including semileptonic decays with light leptons (e, μ) and tau leptons (τ), hadronic states involving excited charm mesons and baryons, as well as decays containing charmonium states. The table also indicates *base* particles (in blue) that form a combination relative to which the input features are computed, and *non-isolated* particles (in red) are those the IMI algorithm must select.

B Selection of prompt particles from excited b -hadron decays

Orbitally and radially-excited b -hadrons (e.g., B_{sJ}^*, B^{**}) frequently decay promptly at the PV, producing high-momentum final-state particles such as the kaon in $B_{s2}^*(5840) \rightarrow B^+ K^-$. Although these particles constitute a small fraction of the overall event content, they

Table 1: Simulated decays used to train the IMI tool. The *base* particles (blue) form a combination relative to which the input features are computed, while the *non-isolated* particles (red) are those the algorithm must select. Labels D^* and Λ_c^{+*} represent cocktails of excited charm-meson and charm-baryon states, respectively. Label ℓ represents either an electron (e) or a muon (μ). The charge conjugate modes are implied.

Base particles	Non-isolated particles	Decay chain
$\bar{D}^0 \ell^+$	π^-	$B^0 \rightarrow D^{*-} \ell^+ \nu_\ell, D^{*-} \rightarrow \bar{D}^0 \pi^-$
$\bar{D}^0 \ell^+$	π^-	$B^0 \rightarrow D^{*-} \tau^+ \nu_\tau, D^{*-} \rightarrow \bar{D}^0 \pi^-, \tau^+ \rightarrow \ell^+ \nu_\ell \bar{\nu}_\tau$
$\bar{D}^0 \tau^+$	π^-	$B^0 \rightarrow D^{*-} \tau^+ \nu_\tau, D^{*-} \rightarrow \bar{D}^0 \pi^-, \tau^+ \rightarrow \pi^+ \pi^- \pi^+ (\pi^0) \bar{\nu}_\tau$
$D^0 \ell^+$	π^-, π^+	$B^+ \rightarrow D^{*0} \ell^+ \nu_\ell, D^{*0} \rightarrow D^{*+} \pi^-, D^{*+} \rightarrow D^0 \pi^+$
$D^0 \ell^+$	π^-, π^+	$B^+ \rightarrow D^{*0} \tau^+ \nu_\tau, D^{*0} \rightarrow D^{*+} \pi^-, D^{*+} \rightarrow D^0 \pi^+, \tau^+ \rightarrow \ell^+ \nu_\ell \bar{\nu}_\tau$
$\bar{D}^0 \ell^+$	π^+, π^-, π^-	$B^0 \rightarrow D^{*-} \ell^+ \nu_\ell, D^{*-} \rightarrow D^{*-} \pi^+ \pi^-, D^{*-} \rightarrow \bar{D}^0 \pi^-$
$\bar{D}^0 \ell^+$	π^+, π^-, π^-	$B^0 \rightarrow D^{*-} \tau^+ \nu_\tau, D^{*-} \rightarrow D^{*-} \pi^+ \pi^-, D^{*-} \rightarrow \bar{D}^0 \pi^-, \tau^+ \rightarrow \ell^+ \nu_\ell \bar{\nu}_\tau$
$D^0 \ell^+$	π^+, π^-, π^-	$B^+ \rightarrow D^{(*)} D_{(s)}^{(*)}, D^{(*)} \rightarrow D^0 \pi^- (\pi^+ \pi^-), D_{(s)}^{(*)} \rightarrow \ell^+ X$
$D^0 \ell^+$	$K^-, 2\pi^-, 2\pi^+$	$B^+ \rightarrow D^{(*)} D_{(s)}^{(*)} K^- \pi^+, D^{(*)} \rightarrow D^0 \pi^- (\pi^+ \pi^-), D_{(s)}^{(*)} \rightarrow \ell^+ X$
$K^+ \ell^-$	ℓ^+	$B^+ \rightarrow K^+ J/\psi, J/\psi \rightarrow \ell^+ \ell^-$
$K^+ \ell^-$	K^+, π^-	$B_s^0 \rightarrow D_s^- \ell^+ \nu_\ell, D_s^- \rightarrow K^+ \pi^- K^-$
$K^+ \ell^-$	K^+, π^-	$B_s^0 \rightarrow D_s^- \tau^+ \nu_\tau, D_s^- \rightarrow K^+ \pi^- K^-, \tau^+ \rightarrow \ell^+ \nu_\ell \bar{\nu}_\tau$
$K^+ \ell^-$	$K^+, 2\pi^-, \pi^+$	$B_s^0 \rightarrow D_s^{*-} \ell^+ \nu_\ell, D_s^{*-} \rightarrow D_s^+ \pi^+ \pi^-, D_s^+ \rightarrow K^+ \pi^- K^-$
$\Lambda_c^+ \ell^-$	$\pi^+ \pi^-$	$\Lambda_b^0 \rightarrow \Lambda_c^{*+} \ell^- \bar{\nu}_\ell, \Lambda_c^{*+} \rightarrow \Lambda_c^+ \pi^+ \pi^-$
$p \ell^-$	$K^- \pi^+$	$\Lambda_b^0 \rightarrow \Lambda_c^+ \ell^- \bar{\nu}_\ell, \Lambda_c^+ \rightarrow p K^- \pi^+$

are critical for precision studies involving missing energy such as searches for LFV in B_s^* decays [12] and relative branching fraction measurements [14].

Owing to their *prompt* origin and *high* momentum, these particles are not efficiently identified by the IMI classifier, which is specifically trained to target displaced tracks from long-lived b -hadron decays. An initial attempt to incorporate them into the IMI training as a separate signal category was explored using inclusive $b\bar{b}$ simulation samples; however, the limited size of available simulation samples at the time prevented meaningful gains in classification performance [36]. While a future version of the IMI tool may revisit this approach using larger and more diverse training data, the current strategy adopts a simple, cut-based selection that exploits the distinctive kinematic features of these prompt decay products.

Three observables are studied to obtain near-orthogonal separation between signal and background:

1. the transverse momentum, p_T , of the track;

2. the perpendicular momentum, p_{\perp} , defined with respect to the reconstructed b -hadron flight direction;
3. particle identification (PID) information, expressed as the logarithm of the likelihood ratio for the kaon versus pion hypotheses, $\Delta \log(\mathcal{L}_{K/\pi})$.

Excited b -hadrons are produced in hard QCD processes and are typically highly boosted. Consequently, their decay products carry large transverse momentum and are emitted almost collinearly with the parent b -hadron trajectory. This effect is particularly pronounced for narrow resonances produced near threshold, where the decay products tend to have small transverse momenta (p_{\perp}). In contrast, background particles originating from the primary vertex through soft QCD interactions generally exhibit lower p_T and a broader angular distribution, resulting in larger p_{\perp} . Moreover, excited b -hadrons containing two heavy quarks (e.g. B_{s2}^*) often decay into a B meson and a kaon, producing a strong kaon PID signal, whereas background particles are predominantly pions. It should be noted that while the requirements p_T of daughter particles from excited b -hadron decays are generally unavoidable for LFV and branching fraction measurements, any hard requirement on p_T in spectroscopy analyses must be applied with care. Such cuts can induce large efficiency variations across the kinematic phase space, making them difficult to model accurately in simulation. In this study, we apply a relatively soft lower bound on p_T , which introduces no significant efficiency shape variations over the invariant mass spectrum of the excited b -hadron candidates (e.g. $m(B^+K^-)$ for B_{sJ}^* studies).

Figure 17 shows, from left to right, the distributions of p_T , p_{\perp} , and $\Delta \log(\mathcal{L}_{K/\pi})$ for signal and background tracks in a simulated $B \rightarrow X_u \mu \nu_{\mu}$ sample where the B meson originates from $B_{s2}^*(5840) \rightarrow B^+K^-$ decays. The bottom panel presents the average number of background particles per event as a function of signal efficiency for three different selection strategies. A cut on p_{\perp} alone does not sufficiently suppress the background, as it leaves too many background particles per event even at high signal efficiency. Introducing an additional requirement on p_T substantially improves background rejection. While the PID observable offers further suppression, it is omitted from the nominal selection to preserve flexibility in defining background-enriched control samples for later analyses. The final two-dimensional selection is:

$$p_T > 400 \text{ MeV}, \quad p_{\perp} < 350 \text{ MeV}.$$

This choice retains over 90% of prompt signal particles while accepting fewer than 0.5 background particles per event.

C Correlation matrix of input features for IMI

Figure 18 shows the correlation matrices of the input variables used in the IMI algorithm, separately for signal and background particles. When a strong correlation appears in one class but not the other, both variables are retained in the training, as each can still contribute complementary information to the classifier. Here we discuss only the most significant correlations (above 50%) observed in both classes.

There is an anti-correlation between the *Transformed* ΔR and *Transformed* $\cos \theta$ variables (defined in Section 3.3), which is more prominent for the signal class than for the background. This is expected since both describe the angular separation between the base

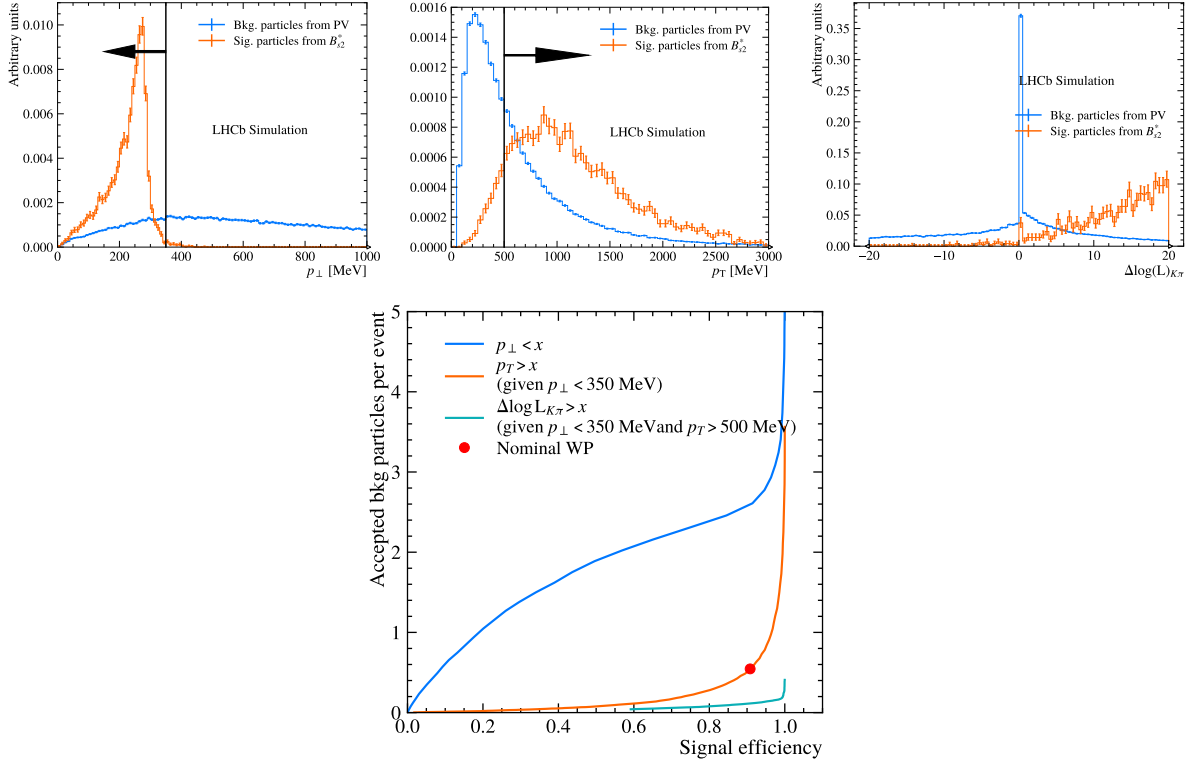


Figure 17: Top row (left to right): Distributions of transverse momentum (p_T), perpendicular momentum (p_\perp), and PID variable $\Delta \log(\mathcal{L}_{K/\pi})$ for particles from prompt decays of excited b -hadrons (orange) and from primary-vertex background (teal) in a simulated Run 3 sample of $B \rightarrow X_u \mu \nu_\mu$ decays. Bottom row: Average number of prompt background particles per event as a function of signal efficiency for three selection scans: (i) $p_\perp < x$; (ii) $p_T > x$ with $p_\perp < 350$ MeV; (iii) $\Delta \log(\mathcal{L}_{K/\pi}) > x$ with $p_T > 500$ MeV and $p_\perp < 350$ MeV. The nominal selection is indicated by the solid black line in the top row and by the red marker in the bottom row.

and extra particle momenta – small ΔR in detector (η, ϕ) space corresponds to a small opening angle and thus large $\cos \theta$ in three-dimensional momentum space, and vice versa. In signal class, extra particles are often kinematically related to the base particles through a common decay, enhancing this relationship, whereas in background events they are largely uncorrelated, diluting the pattern. We include both variables in the training because, despite their correlation, they probe angular separation in complementary coordinate systems, allowing the classifier to exploit subtle differences in signal and background topologies.

Additionally, a moderate correlation is observed between $\log(\chi_{\text{IP wrt. SV}}^2)$ and $\log(\chi_{\text{DOCA}}^2)$. This is expected since both quantify spatial compatibility of the extra particle with the base candidate: a small DOCA between the extra and base particle trajectories typically corresponds to a small impact parameter with respect to the secondary vertex, and vice versa. We include both variables in the training because they capture different geometric aspects: χ_{DOCA}^2 measures the distance between the two particles, while $\chi_{\text{IP wrt. SV}}^2$ quantifies how well the extra particle is consistent with the secondary vertex reconstructed from the base particles.

Importantly, when we evaluated the signal efficiency across different exclusive channels,

we observed a small but consistent improvement from retaining these two sets of correlated variables, compared to removing one from each pair.

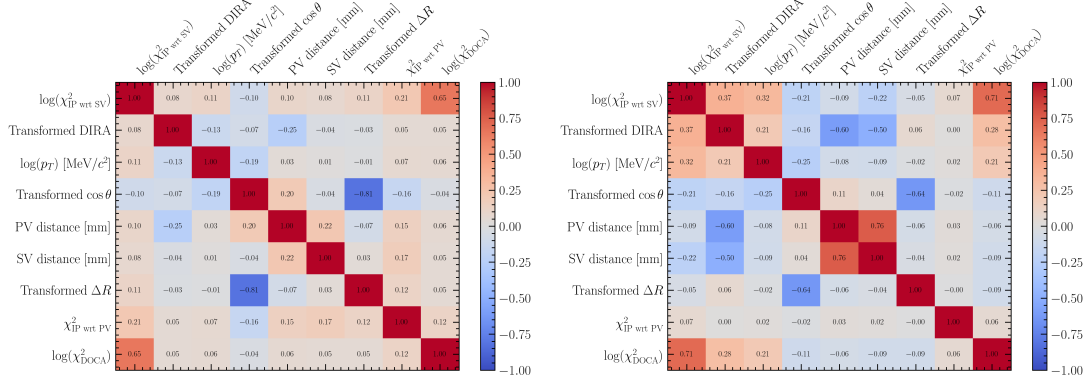


Figure 18: Correlation matrices of the input variables used in the IMI algorithm, shown for signal (left) and background (right) particles.

D Signal and background efficiency as a function of isolation variables

Figures 19 shows the signal efficiency and background rejection as a function of the isolation score for the three algorithms: track, cone, and IMI. These have been evaluated using the simulated cocktail samples shown in Table 1, which include a variety of b -hadron decay modes and kinematic configurations.

For track isolation, the discriminating variable is $\chi^2_{\text{IP wrt PV}} \geq x$ or the **samePV** flag. The binary nature of the **samePV** flag sets the baseline signal efficiency and background rejection, while threshold x determines further discrimination. When the threshold x is very small, most tracks are retained, leading to a high signal efficiency but low background rejection. Increasing x tightens the selection, reducing the signal efficiency while improving the background rejection.

For cone isolation, the relevant variable is $\Delta R < y$. An extremely small y accepts only tracks very close in (η, ϕ) to the base particle, yielding low signal efficiency but strong background rejection. As y increases, more tracks are accepted, resulting in higher signal efficiency but reduced background rejection.

For IMI isolation, the discriminating variable is $\text{IMI} > z$. Small values of z accept most candidates, giving high signal efficiency but low background rejection. Raising z increases the strictness of the selection, thereby lowering the signal efficiency and increasing the background rejection.

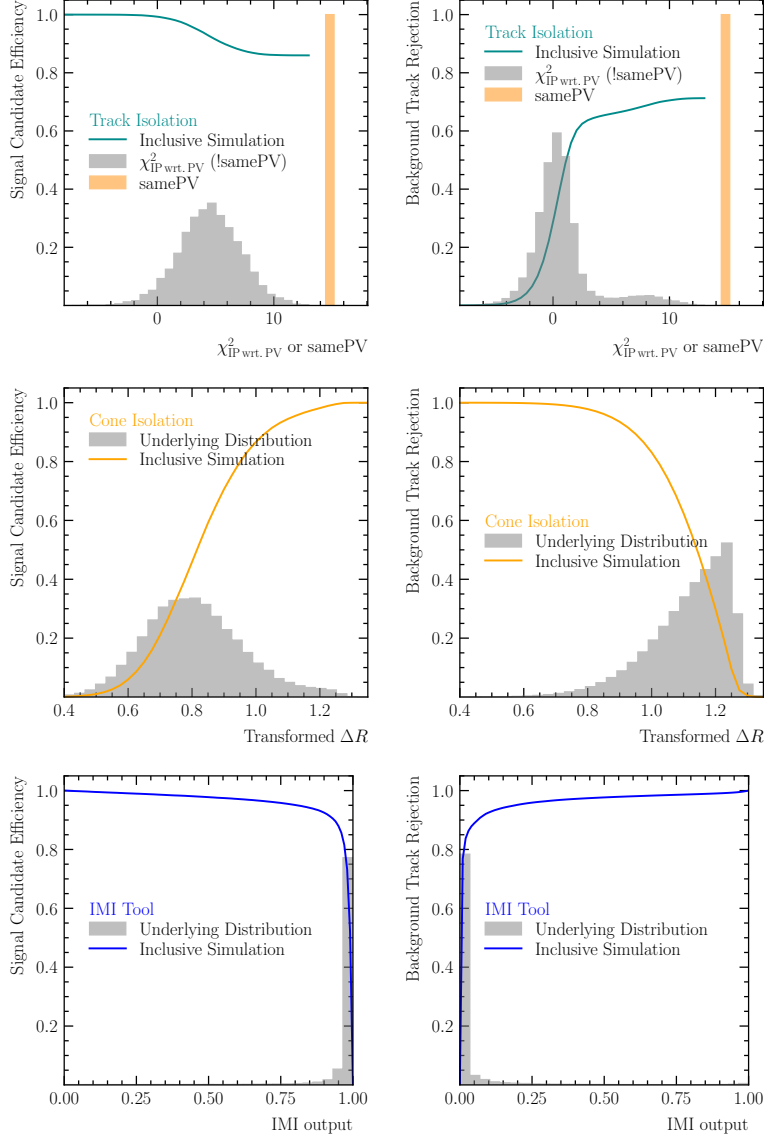


Figure 19: Signal efficiency (first column) and background rejection (second column) as a function of the isolation variables for the track (top row), cone (middle row), and IMI (bottom row) algorithms.

References

- [1] LHCb collaboration, R. Aaij *et al.*, *The LHCb Upgrade I*, [arXiv:2305.10515](#), to appear in JINST.
- [2] R. Aaij *et al.*, *Allen: A high level trigger on GPUs for LHCb*, *Comput. Softw. Big Sci.* **4** (2020) 7, [arXiv:1912.09161](#).
- [3] LHCb collaboration, M. Saur, *LHCb HLT2: Real-time alignment, calibration, and software quality-assurance*, *PoS ICHEP2022* (2023) 685.
- [4] N. Schulte *et al.*, *Development of the Topological Trigger for LHCb Run 3*, [arXiv:2306.09873](#).

- [5] R. Aaij *et al.*, *Computing Model of the Upgrade LHCb experiment*, doi: 10.17181/CERN.Q0P4.57ON.
- [6] R. Aaij *et al.*, *Tesla : an application for real-time data analysis in High Energy Physics*, Comput. Phys. Commun. **208** (2016) 35, [arXiv:1604.05596](#).
- [7] R. Aaij *et al.*, *A comprehensive real-time analysis model at the LHCb experiment*, JINST **14** (2019) P04006, [arXiv:1903.01360](#).
- [8] A. Abdelmotteleb *et al.*, *The LHCb Sprucing and Analysis Productions*, [arXiv:2506.20309](#).
- [9] LHCb collaboration, P. Li, *Real-time analysis in Run 3 with the LHCb experiment*, PoS **EPS-HEP2021** (2022) 829.
- [10] LHCb collaboration, R. Aaij *et al.*, *The LHCb Upgrade I*, JINST **19** (2024) P05065, [arXiv:2305.10515](#).
- [11] LHCb collaboration, R. Aaij *et al.*, *Test of lepton flavor universality using $B0 \rightarrow D^{*-}\tau + \nu\tau$ decays with hadronic τ channels*, Phys. Rev. D **108** (2023) 012018, [arXiv:2305.01463](#), [Erratum: Phys.Rev.D 109, 119902 (2024)].
- [12] LHCb collaboration, R. Aaij *et al.*, *Measurement of the ratios of branching fractions $R(D^{*})$ and $R(D^0)$* , Phys. Rev. Lett. **131** (2023) 111802, [arXiv:2302.02886](#).
- [13] LHCb collaboration, R. Aaij *et al.*, *Determination of the quark coupling strength $|V_{ub}|$ using baryonic decays*, Nature Phys. **11** (2015) 743, [arXiv:1504.01568](#).
- [14] LHCb collaboration, R. Aaij *et al.*, *Measurement of the relative $B^{-} \rightarrow D^0/D^{*0}/D^{**0} \mu^{-} \bar{\nu}_{\mu}$ branching fractions using B^{-} mesons from \bar{B}_s^{*0} decays*, Phys. Rev. D **99** (2019) 092009, [arXiv:1807.10722](#).
- [15] D0 collaboration, V. M. Abazov *et al.*, *Search for $B_s \rightarrow \mu^{+}\mu^{-}$ at D0*, Phys. Rev. D **76** (2007) 092001, [arXiv:0707.3997](#).
- [16] CDF collaboration, T. Aaltonen *et al.*, *Search for $B_s^0 \rightarrow \mu^{+}\mu^{-}$ and $B^0 \rightarrow \mu^{+}\mu^{-}$ Decays with the Full CDF Run II Data Set*, Phys. Rev. D **87** (2013) 072003, [arXiv:1301.7048](#), [Erratum: Phys.Rev.D 97, 099901 (2018)].
- [17] ATLAS collaboration, G. Aad *et al.*, *Search for the decay $B_s^0 \rightarrow \mu\mu$ with the ATLAS detector*, Phys. Lett. B **713** (2012) 387, [arXiv:1204.0735](#).
- [18] CMS collaboration, S. Chatrchyan *et al.*, *Search for $B(s)$ and B to dimuon decays in pp collisions at 7 TeV*, Phys. Rev. Lett. **107** (2011) 191802, [arXiv:1107.5834](#).
- [19] D. Martinez, J. A. Hernando, and F. Teubert, *LHCb potential to measure/exclude the branching ratio of the decay $B_s \rightarrow \mu^{+}\mu^{-}$* , <https://cds.cern.ch/record/1027522>. CERN Report No. LHCb-2007-033, 2007.
- [20] LHCb collaboration, B. Adeva *et al.*, *Roadmap for selected key measurements of LHCb*, [arXiv:0912.4179](#).

- [21] LHCb collaboration, R. Aaij *et al.*, *Opposite-side flavour tagging of B mesons at the LHCb experiment*, Eur. Phys. J. **C72** (2012) 2022, [arXiv:1202.4979](#).
- [22] LHCb collaboration, R. Aaij *et al.*, *LHCb detector performance*, Int. J. Mod. Phys. **A30** (2015) 1530022, [arXiv:1412.6352](#).
- [23] LHCb collaboration, R. Aaij *et al.*, *First observation of $\bar{B}_s^0 \rightarrow D_{s2}^{*+} X \mu^- \bar{\nu}$ decays*, Phys. Lett. **B698** (2011) 14, [arXiv:1102.0348](#).
- [24] L. Gavardi, *Search for lepton flavour violation in τ decays at the lhcb experiment*, <https://repository.cern/records/d587q-3h630>. PhD thesis, Università degli Studi di Milano-Bicocca, CERN-THESIS-2013-259, 2013.
- [25] ATLAS collaboration, M. Aaboud *et al.*, *Study of the rare decays of B_s^0 and B^0 mesons into muon pairs using data collected during 2015 and 2016 with the ATLAS detector*, JHEP **04** (2019) 098, [arXiv:1812.03017](#).
- [26] CMS collaboration, A. Tumasyan *et al.*, *Measurement of the $B_s^0 \rightarrow \mu^+ \mu^-$ decay properties and search for the $B^0 \rightarrow \mu^+ \mu^-$ decay in proton-proton collisions at $\sqrt{s} = 13$ TeV*, Phys. Lett. B **842** (2023) 137955, [arXiv:2212.10311](#).
- [27] LHCb collaboration, R. Aaij *et al.*, *Precision measurement of forward Z boson production in proton-proton collisions at $\sqrt{s} = 13$ TeV*, JHEP **07** (2022) 026, [arXiv:2112.07458](#).
- [28] CDF collaboration, T. Aaltonen *et al.*, *Measurement of the inclusive jet cross section at the Fermilab Tevatron Collider Using a Cone-Based Jet Algorithm*, Phys. Rev. D **78** (2008) 052006, [arXiv:0807.2204](#), [Erratum: Phys.Rev.D 79, 119902 (2009)].
- [29] LHCb collaboration, R. Aaij *et al.*, *Identification of charm jets at LHCb*, JINST **17** (2022) P02028, [arXiv:2112.08435](#).
- [30] LHCb collaboration, R. Aaij *et al.*, *A precise measurement of the B^0 meson oscillation frequency*, Eur. Phys. J. **C76** (2016) 412, [arXiv:1604.03475](#).
- [31] ATLAS collaboration, M. Aaboud *et al.*, *Measurement of the tau lepton reconstruction and identification performance in the atlas experiment using pp collisions at $\sqrt{s} = 13$ tev*, <https://cds.cern.ch/record/2261772>. ATLAS-CONF-2017-029, CERN, Geneva, 2017.
- [32] CMS collaboration, A. Tumasyan *et al.*, *Cms strategies for tau reconstruction and identification using particle-flow techniques*, <https://cds.cern.ch/record/1198228>. CMS-PAS-PFT-08-001, CERN, Geneva, 2009.
- [33] LHCb collaboration, R. Aaij *et al.*, *Measurement of the ratio of branching fractions $\mathcal{B}(\bar{B}^0 \rightarrow D^{*+} \tau^- \bar{\nu}_\tau) / \mathcal{B}(\bar{B}^0 \rightarrow D^{*+} \mu^- \bar{\nu}_\mu)$* , Phys. Rev. Lett. **115** (2015) 111803, Publisher's Note *ibid.* **115** (2015) 159901, [arXiv:1506.08614](#).
- [34] S. A. Braun, *Measurement of the CKM matrix elements $|V_{ub}|/|V_{cb}|$ from semileptonic B_s^0 decays.*, PhD thesis, U. Heidelberg (main), U. Heidelberg (main), 2020, doi: 10.11588/heidok.00028524.

- [35] T. Chen and C. Guestrin, *XGBoost: A Scalable Tree Boosting System*, doi: 10.1145/2939672.2939785 arXiv:1603.02754.
- [36] L. Hartman, *ML-based charged isolation tool for Run 3 and a comparative assessment*, <https://repository.cern/records/wx8gk-hs282>, 2023. [CERN-STUDENTS-NOTE-2023-238; accessed 19-Aug-2023].
- [37] T. Akiba *et al.*, *Optuna: A Next-generation Hyperparameter Optimization Framework*, arXiv:1907.10902.
- [38] S. M. Lundberg and S. Lee, *A unified approach to interpreting model predictions*, CoRR **abs/1705.07874** (2017) arXiv:1705.07874.
- [39] A. Mathad *et al.*, *FunTuple: A New N-tuple Component for Offline Data Processing at the LHCb Experiment*, Comput. Softw. Big Sci. **8** (2024) 6, arXiv:2310.02433.
- [40] *Rec project*, <https://gitlab.cern.ch/lhcb/Rec>. [Online; accessed 19-Aug-2023].
- [41] W. Sutcliffe *et al.*, *Scalable Multi-Task Learning for Particle Collision Event Reconstruction with Heterogeneous Graph Neural Networks*, arXiv:2504.21844.
- [42] LHCb collaboration, V. Vagnoni, T. Gershon, and G. Punzi, *Technology developments for LHCb Upgrade II*, arXiv:2504.03088.
- [43] L. LHCb collaboration, *LHCb Upgrade II Scoping Document*, CERN, Geneva, 2024. doi: 10.17181/CERN.2RXP.HDK0.